# CONTROLLED SPALLING IN (100)-ORIENTED GERMANIUM BY ELECTROPLATING

by

Dustin Ray Crouse

A thesis submitted to the Faculty and the Board of Trustees of the Colorado School of Mines in partial fulfillment of the requirements for the degree of Master of Science (Materials Science).

Golden, Colorado

Date ___________________________

Signed: _____________________________________

Dustin R. Crouse

Signed: _____________________________________

Dr. Corinne E. Packard
Thesis Advisor

Golden, Colorado

Date ___________________________

Signed: ___________________________

Dr. Ryan O'Hayre

Professor and Head of

Materials Science Program

ABSTRACT

This work investigates controlled spalling as a method to exfoliate thin films of various thickness from rigid, crystalline germanium (Ge) substrates and to enable substrate reuse for III-V single junction photovoltaic devices. Technological limitations impeding wide-spread adoption of flexible electronics and high-material-cost photovoltaic devices have motivated significant interest in a method to remove devices from their substrates. DC magnetron sputtering has been previously utilized to remove semiconductor devices of various thicknesses from Ge substrates, but this method is expensive and time-consuming. Controlled spalling via high-speed electrodeposition is a fast, inexpensive exfoliation method that utilizes a tensile-stressed metal layer deposited on a (100)-oriented Ge substrate and an external force to mechanically propagate a crack parallel to the surface at a desired depth in the substrate material. Suo and Hutchinson's quantitative models describe critical combinations of film thickness and strain mismatch between a film and substrate at which a stressed bilayer system spontaneously spalls; however, fine control over a wide steady-state spall depth range has been limited by the ability to experimentally tailor strain mismatch caused by residual stress within deposited stressor layers. This work investigates the effect of tuning electroplating current density and electrolyte chemistry on the residual stress in a nickel stressor film and their impact on the achievable spall depth range. Steady-state spall depth is found to increase with increasing stressor layer thickness and decrease with increasing residual stress. By tailoring residual stress through adjusting plating conditions and the electrolyte's phosphorous concentration, wide control over spall depth within Ge substrates from sub-micron to ~76μm-thicknesses were achieved.

To assess the viability of utilizing controlled spalling for substrate reuse, this dissertation

demonstrates the first III-V solar cells (GaInAsP, $E_g$~1.7 eV) grown directly on a spalled-Ge substrate without any additional surface preparation. Widespread adoption of high-efficiency III-V solar cells has been limited by expensive deposition processes and high material cost of substrates. Substrate reuse offers a promising route towards enabling III-V devices to become cost-competitive for one-sun terrestrial applications. In this study, the quality of spalled Ge surfaces is characterized to assess lattice matching capability between the device layer materials and the substrate. GaAs films grown on spalled Ge substrates by hydride vapor phase epitaxy were single-crystal in nature. III-V solar cells grown on spalled and pristine Ge substrates show nearly equivalent efficiency of ~8%, despite the roughness of the spalled-Ge substrate. Principles of fractography were used to deduce that surface roughness originated from non-uniform crack propagation and mixed-mode loading during the spalling process.

TABLE OF CONTENTS

ABSTRACT… iii

TABLE OF CONTENTS v

LIST OF FIGURES viii

LIST OF TABLES xi

ACKNOWLEDGEMENTS xii

CHAPTER 1 INTRODUCTION 1

1.1 Controlled Spalling 2

1.2 Substrate Reuse Applications for III-V Photovoltaics 6

1.3 Thesis Layout 8

CHAPTER 2 EFFECTS OF ELECTROPLATING BATH CHEMISTRY ON CONTROLLED SPALLING IN (100)-ORIENTED GE SUBSTRATES 10

2.1 Author Contributions 10

2.2 Manuscript - Abstract 11

2.3 Manuscript - Introduction 12

2.4 Manuscript – Experimental Methods 15

2.5 Manuscript – Results and Discussion 17

2.6 Manuscript - Conclusion 26

CHAPTER 3 III-V SOLAR CELLS GROWN ON REUSABLE GE SUBSTRATE 27

3.1 Author Contributions ... 27

3.2 Manuscript - Abstract ... 28

3.3 Manuscript - Introduction ... 29

3.4 Manuscript – Experimental Methods ... 30

3.5 Manuscript – Results and Discussion ... 31

3.5.1 Controlled Spalling of Ge Thin-Films from Ge Substrate ... 31

3.5.2 GaInAsP Solar Cell Growth on Spalled-Ge by HVPE ... 33

3.6 Manuscript – Conclusion ... 35

CHAPTER 4 FRACTURE PATTERNS ON SPALLED (100)-GERMANIUM SURFACES ... 36

4.1 Macro-scale Fracture Behavior ... 37

4.2 Steady-state Region: Surface Roughness ... 39

4.3 Arrest Lines ... 41

4.4 Edge-affected Zones ... 43

4.4.1 River Line Patterns ... 44

4.4.2 Twist Hackle ... 47

4.4.3 Mixed Mode Loading Conditions ... 48

4.5 Chapter Summary ... 50

CHAPTER 5 SUMMARY AND CONCLUSIONS ... 51

5.1 Effects of Bath Chemistry and Plating Parameters on Spall Depth ... 51

5.2 Substrate Reuse for Photovoltaics Applications ........ 52

5.3 Fractography of Spalled (100)-Oriented Ge ........ 53

BIBLIOGRAPHY ........ 55

APPENDIX A CAD FILES FOR ELECTROPLATING JIG ........ 59

APPENDIX B MATHEMATICA MODELS OF LINEAR ELASTIC SPONTANEOUS FRACTURE IN GERMANIUM SUBSTRATES ........ 62

APPENDIX C MATLAB FILES FOR LASER PROFILOMETRY DEPTH ANALYSIS ........ 70

LIST OF FIGURES

Figure 1.1: (a) Spalling in (100) GaAs substrates results in faceting along {110} planes, which causes excess material waste due to non-planar, faceted, crack propagation (b) Fracture along (100) planes in (100)-Ge ideally leads to a planar, featureless surface and does not consume additional material due to faceting ............................ 4

Figure 1.2: Theoretical loading conditions used to predict steady state crack depth (λ) as adapted from Suo & Hutchinson [13]......................................................................... 5

Figure 1.3: Process flow to demonstrate spalling-enabled wafer reuse by high-throughput deposition of III-V materials. (a) A (100)-Ge substrate is electroplated with stressed nickel, (b) an adhesive handle is attached and pulled to initiate a spalling fracture, and (c) III-V layers are epitaxially grown via HVPE on a Ni-etched spalled Ge substrate ........................................................................................ 7

Figure 2.1: Controlled spalling conditions for Watts Nickel, 5mM $H_3PO_3$, and 10mM $H_3PO_3$ bath chemistries emphasized with fitted trend lines ................................................ 18

Figure 2.2: (left) Ge substrate with a 1.5mm exclusion zone following controlled spalling and (right) its associated exfoliated Ge/Ni film with the Ge side exposed. Letter ‘P’ represents the orientation and alignment of features at matching areas of the substrate and film............................................................................................... 19

Figure 2.3: SEM micrograph of a cross-sectioned spalled film showing the thickness of spalled Ge and electroplated Ni deposited using the 5mM $H_3PO_3$ chemistry........... 20

Figure 2.4: (a) Theoretical and experimental Ge spall depth as a function of stressor layer thickness for each bath chemistry (b) The phosphorous based chemistries significantly reduced spall depths.................................................................... 22

Figure 2.5: A Ge substrate electroplated in 10mM chemistry after granular spalling................. 21

Figure 2.6: Stress measurements for each chemistry plated under controlled spalling conditions. Increasing phosphorous content drastically increases residual tension. . 24

Figure 3.1: (a) Representation of spalling process to remove thin Ge-film from Ge substrate and (b) device schematic of GaInAsP solar cell grown on spalled-Ge substrate ...... 31

Figure 3.2: Cross-sectional SEM image representative of spalled-Ge film attached to the electroplated Ni stressor layer post spalling process ................................................ 32

Figure 3.3: (a) Plan-view optical image of spalled Ge substrate with a 2-mm wide exclusion zone along the perimeter and (b) a representative 25µm x 25µm AFM scan in the sample center area. ........................................................................................ 32

Figure 3.4: (a) Wide-angle 2-theta XRD pattern for GaAs epitaxial films grown on bulk Ge and spalled-Ge substrate suggesting single crystal growth maintained on spalled-Ge (graphs shifted in y-axis for clarity), (b) plan-view optical image showing morphology of spalled-Ge substrate before and after ~1.5µm GaAs growth. ......................................................................................................... 33

Figure 3.5: (a) EQE and (b) JV characteristic of GaInAsP heterojunction solar cells grown on spalled-Ge (red) and epi-ready bulk Ge substrate (blue) highlighting nearly equivalent performance. An optimized GaInAsP homojunction device with front passivation and lower base doping grown on GaAs is also shown to highlight potential knobs for performance improvement. (c) Dark lock-in thermography images at 1V reverse bias voltage reveal no localized defects or heating spots........ 34

Figure 4.1: (top) color height map of a spalled Ge substrate where higher z values correspond to deeper areas relative to the original surface and (bottom) a line scan positioned at the dashed line through the sample center with regions of interest highlighted .... 38

Figure 4.2: Line scans of the steady-state regions in 10 samples plated and spalled under the same conditions show significant spall depth changes between the sample center and the region edge ......................................................................................... 39

Figure 4.3: a) A representative laser scan of a spalled surface at the sample center, b) the same surface after form removal, and c) the surface profile across two undulations which intersect the red-dashed line in (b) ............................................. 41

Figure 4.4: (a) Top-down SEM view of two arrest lines on spalled Ge and (b) a representative cross section view of the same surface (not to scale). Low angle planes define the arrest line and fractured surfaces on each side of an arrest front lie on a different plane. ........................................................................................................... 42

Figure 4.5: Ge substrates spalled from two different directions. Black arrows represent crack propagation direction and white arrows represent orientation of the generated undulations ................................................................................................... 43

Figure 4.6: Digital micrographs of fractured surfaces showing (a) the top-left corner of a spalled region, (b) merging of river patterns with distance away from an arrest line, (c) high magnification of river patterns, and (d) river line patterns extending through arrest lines ........ 46

Figure 4.7: River patterns on fracture surface of epoxy resin tested in mixed-mode I/III loading as adapted from Ref. [51] ........ 45

Figure 4.8: Twist hackle formed at a plated edge oriented perpendicular to main spalling direction (or mode I component) but parallel with the local mode III component.... 48

Figure 4.9: General twist hackle generation from mixed-mode loading as adapted from Ref. [57]. Local direction of fracture is aligned with the mode III component......... 48

Figure 4.10: The relative magnitude of tensile stress components at different locations within the deposited Ni layer from a planar view (a) and a cross section view (b).............. 49

Figure 4.11: Schematic of moments induced on plated substrates at spalling fracture initiation. Purple arrows represent crack propagation direction and red arrows represent the moments induced by the roller and anisotropic stress states within the Ni film. ...... 50

Figure A.1: Part assembly for electroplating jig used to hold 2cm x 2cm wafer........................ 60

Figure A.2: SolidWorks drawing file demonstrating electroplating jig dimensions in different views. ........ 61

Figure A.3: SolidWorks drawing file demonstrating electroplating jig cover dimensions……...62

LIST OF TABLES

Table 2.1: Measured Ni film thicknesses and Ge spall depth for control-spalled samples at various current densities ........................................................................................ 21

Table 4.1: Representative roughness measurements over 8-mm x 8-mm spalled areas before and after form removal ........................................................................................ 40

ACKNOWLEDGEMENTS

First, I would like to thank the Metallurgical and Materials Engineering Department, as well as the Department of Energy's Office of Renewable Energy and Efficiency, which provided funding for this research under Sunshot's Next Generation Photovoltaics funding program (Contract No. DE-EE00028395). My advisor, Dr. Corinne Packard, has been an exemplary mentor and has been a model for how to approach problems from multiple perspectives. Her guidance has made me a more thoughtful researcher and drastically improved my communication skills. It was an honor collaborating with our team at NREL who provided materials, project guidance, and device growth. Nikhil Jain was critical in growing III-V solar cells on spalled Ge-substrates. I would like to especially thank John Simon and Kevin Schulte for their XRD expertise. Aaron Ptak and David Young provided key feedback to improve the electroplating and spalling processes.

I have been fortunate to have mentored and worked with several very productive and passionate undergraduate assistants. Chloe Castaneda provided expert AFM characterization and training as a 2015 REMRSEC REU intern. Thanks to Jacob Tavenner for his insightful suggestions to improve the spalling process and genuine excitement for the project. Anna Braun, a 2016 REMRSEC REU intern, invaluably progressed the project forward through prototyping and calibrating the spalling jig 2.0, Keyence microscopy, sample preparation, and extensive laboratory work.

I truly appreciate the support and contributions from my friends and colleagues. Taylor Wilkinson and Dong Wu performed nano-indentation measurements to determine reduced modulus. Noor Alkurd provided field emission SEM micrographs of several samples and was a

great friend I could always count on for interesting discussions in middle-eastern culture or baking escapades. Matt Musselman was always there for publishing guidance and Rosalie O'Brien helped me to maintain balance and perspective throughout this process. Finally, thank you to everyone who helped in editing and supporting me throughout this endeavor.

# CHAPTER 1 INTRODUCTION

Over the past few decades, the process of removing semiconductor devices and high-performance electronics from mechanically rigid substrates has seen significant technological development. Conventionally, integrated circuits and photovoltaic devices are fabricated on thick crystalline substrates. As attention toward flexible electronics gains prominence, a method which can reliably exfoliate (or delaminate) thin devices fabricated on rigid support structures is required. Furthermore, lift-off can enable substrate reuse for technologies limited by high material cost, such as III-V photovoltaics.

Several methods have demonstrated removal of thin films, integrated circuits, light emitting diodes, and photovoltaic devices from bulk substrates; however, each suffer drawbacks which prevent widespread adoption. Chemical etching of sacrificial release layers has been used to epitaxially lift off III-V devices and Schottky diodes, but the process involves hazardous HF acid and low throughput due to slow lateral etch rates. [1]–[4] The SLIM-CUT technique can be used to exfoliate films by exploiting mismatches in the coefficients of thermal expansion between substrates and a metal stressor layer to induce spontaneous fracture, but the process requires high-temperature annealing and has been shown to cause microstructural defects. [5], [6] Several methods weaken the substrate material to mechanically initiate a crack at a specific depth, but strong acids, expensive equipment, or additional processing is often required. For example, electrochemical etching to produce a weakened porous layer within the substrate involves both HF acid and a surface reformation step. [7] Silicon-on-insulator wafers produced by SmartCut and MEMC Electronic Materials, Inc.'s methods demonstrate that thin, single-crystal silicon can be delaminated in a way that is sufficiently repeatable and reliable for the high demands of the

semiconductor industry; [8] however, the ion implantation to produce a weakened layer within the substrate requires costly high-vacuum implantation equipment and high-temperature annealing. [8], [9]

The motivation for this work is to utilize a safe, inexpensive exfoliation method which allows substantial control over film thickness and enables wafer reuse for (100)-oriented germanium (Ge). Subsection 1.1 introduces controlled spalling, a versatile exfoliation method by which fracture mechanics can be exploited to produce thin bilayer films. This study is also one facet of a project led by the National Renewable Energy Laboratory (NREL). The collaboration, explained in sub-section 1.2, demonstrates that high-speed epitaxial growth combined with device lift-off and substrate reuse technology is technologically feasible and a potential route to reduce the cost of high-performance photovoltaic devices. Finally, sub-section 1.3 provides a brief layout of the work presented in this thesis.

## 1.1 Controlled Spalling

Controlled spalling via electrodeposition is an inexpensive lift-off method which can be performed at room temperature without vacuum equipment. It is a recently developed technique that has the promise of much higher throughput compared to conventional lift-off methods and does not involve the use of hazardous acids. The process takes only minutes to complete, can be easily integrated into fabrication lines, and extended to any commercially available crystalline wafers. One spalling technique by Bedell et al. utilized DC magnetron sputtering to demonstrate spalling of single-junction III–V PV devices from a Ge substrate. However, this lift-off method required expensive sputtering equipment and the deposition of 6μm-thick Ni films at an optimal 5mTorr would require >2 hours. [10] The spalling technique in this study utilizes high-speed electroplating to deposit stressed films at very fast rates (1-5 min). Electrodeposition is a well-established technique wherein plating

conditions and bath chemistry are typically tuned to minimize residual stresses within the film. [11], [12] The scalability of this process is evident by the commercial use of low-capital equipment and materials in decorative coating, corrosion resistance, and electroforming applications. [11] Thickness of the deposits can be easily controlled in the sub-micron range and is routinely used to close vias for interconnecting chip layers as well as for defining gridlines on solar cells. Although controlled spalling has not been demonstrated on a commercial scale, evidence of mechanically delaminating single-crystal semiconductor layers without introducing detrimental defects is abundant in the semiconductor industries. Once initiated, spalling is nearly instantaneous compared to the hours required for etching-based lift-off techniques. Thus, the entire process, including electroplating, handling, and spalling, takes only a few minutes from start to finish.

Controlled spalling utilizes fracture in a controlled manner to propagate a crack at a desired depth in the substrate material. Spalling occurs when strain mismatch between a tensile-stressed film and the substrate is sufficient to surpass the substrate's fracture toughness. [13] Two components of the stress field, the $K_I$ 'opening mode' component and the $K_{II}$ 'shear mode' component, along with an externally applied force act together to initiate fracture. [13], [14] The crack propagates at a depth where the $K_I$ stress intensity is sufficient to break bonds in the substrate and where the $K_{II}$ stress intensity becomes zero. Controlled spalling fracture follows the plane that is oriented such that the shear-mode stress intensity is minimized. Ideally, a stressed film generates a subsurface fracture parallel to the substrate surface at a depth guided by the stress field ahead of the crack front. When the cleavage plane is not oriented parallel to the substrate surface, however, faceting can occur and lead to significant material waste, represented as Figure 1.1(a). [15] In the case of spalled (100)-oriented GaAs wafers, cleavage is preferred along complementary sets of {110} planes which was demonstrated as ~5-50µm facets. [16], [17] Conversely, if a weak plane

is oriented parallel to the steady-state spalling depth, then fracture along that plane has the potential to create a featureless, planar surface. For the (100)-oriented Ge substrates used in this study, an initiated crack follows a (100) plane thereby cleaving parallel to the substrate surface and ideally leading to uninterrupted surface, see Figure 1.1(b). [18] By exploiting orientation of preferred crystallographic planes, Ge has the potential to produce far less material waste compared to (100)-oriented GaAs.

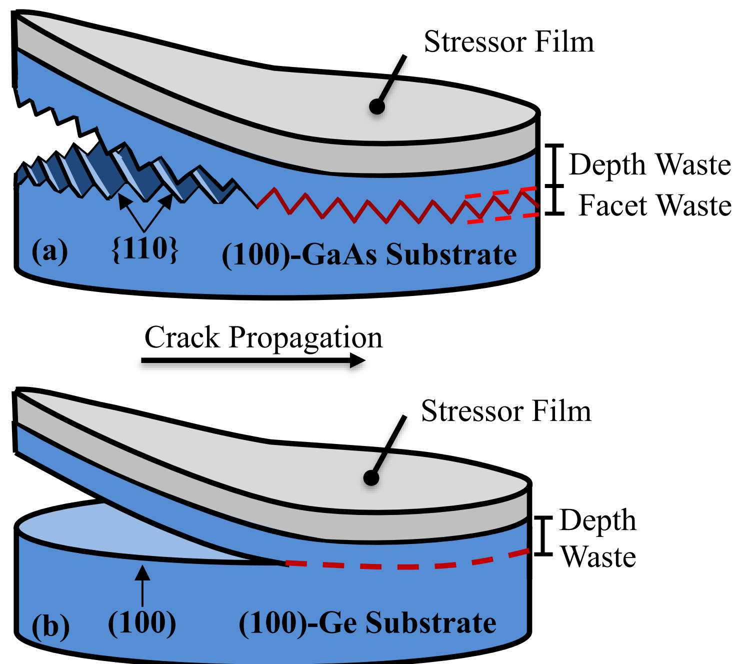


Figure 1.1: (a) Spalling in (100) GaAs substrates results in faceting along {110} planes, which causes excess material waste due to non-planar, faceted, crack propagation (b) Fracture along (100) planes in (100)-Ge ideally leads to a planar, featureless surface and does not consume additional material due to faceting

Suo and Hutchinson pioneered theoretical models that are used in this research to describe critical combinations of film thickness and external loads conditions at which a stressed film/substrate system delaminates. [13], [14] They determined the stress field induced by strain mismatch between the film and substrate is the same as that produced during edge loading. A schematic of the theoretical model is shown as Figure 1.2 (see page 5)in which the two materials

are assumed infinitely long and the crack is semi-infinite. The structures behind the crack are considered two composite beams subjected to longitudinal loading $P$ and moment $M$ acting about the neutral axis of each of them. Suo and Hutchinson found the steady-state crack depth (λ) was extremely sensitive to the ratio of stressor film and substrate thickness ($h_{Ni}/\lambda_0$) and the stiffness ratio between the two materials (α), which is expressed as

$$\alpha = \frac{(\bar{E}_f - \bar{E}_s)}{(\bar{E}_f + \bar{E}_s)} \tag{1.1}$$

where $\bar{E}_i = E_i(1 - v_i^2)$ in plane strain. This study uses the model by enforcing $K_{II} = 0$ to solve a general equation governing steady-state depth of a subsurface crack propagating parallel to the surface. The depth values were then used to solve for the appropriate opening-mode $K_I$ stress intensity. Finally, letting $K_I$ equal to the substrate fracture toughness $K_{IC}$, critical combinations of stressor layer thickness ($h_{Ni}$) and residual stress within the film ($\sigma$) could be determined. Chapter 2 further addresses methods for tuning these parameters to control the depth of the fracture and compares experimental results with theoretical predictions developed using this model.

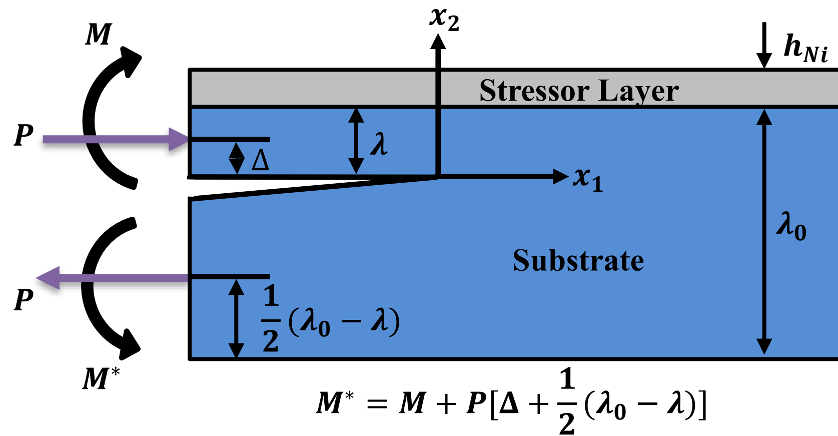


Figure 1.2: Theoretical loading conditions used to predict steady state crack depth (λ) as adapted from Suo & Hutchinson [13]

## 1.2 Substrate Reuse Applications for III-V Photovoltaics

One application of this research in photovoltaics was studied by capitalizing on NREL's III-V solar cell expertise. III-V solar cells based on Ge substrates will face severe challenges meeting the Department of Energy's (DOE) SunShot price goal of 9¢/kWh by the year 2020. These compound semiconductor-based devices hold world-record efficiencies for both single- and multi-junction solar cells. [19] However, expensive deposition processes and the high material cost of substrates have limited their widespread use in one-sun terrestrial applications. One plausible strategy for low-cost device fabrication addresses high costs of these semiconductor platforms via substrate reuse methods. A recent techno-economic analysis of III-V device production revealed substrate reuse enabled by controlled spalling has the greatest impact on cost reductions. [20] The cost per III-V device after 10 reuses without chemo-mechanical polishing (CMP) between cycles was estimated at $37 using conventional metalorganic vapor phase epitaxy to deposit the cells, which is a substantial cost reduction compared to $165 per cell in the absence of substrate reuse. Spalling has been used to remove photovoltaic devices from Si and Ge substrates at various thicknesses with minimal wafer material consumption and no significant performance degradation compared to non-spalled devices. [21]–[25] A previous collaboration between NREL and Colorado School of Mines (CSM) similarly demonstrated that GaAs solar cells can be spalled from GaAs wafers without loss in performance. [16] However, few have reused spalled substrates as a platform to grow a functioning III-V device without additional surface preparation such as CMP. Successful growth of III-V devices on as-spalled substrates is essential for demonstrating the feasibility of substrate reuse.

The specific focus of this collaborative project with NREL was the fabrication of high-quality GaInAsP solar cells lattice-matched to spalled Ge substrates. The proposed fabrication process to achieve this goal is schematically shown in Figure 1.3. Since device layer materials are

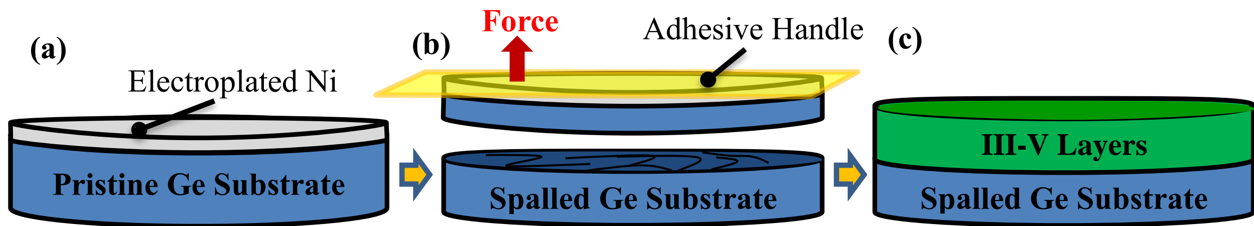


Figure 1.3: Process flow to demonstrate spalling-enabled wafer reuse by high-throughput deposition of III-V materials. (a) A (100)-Ge substrate is electroplated with stressed nickel, (b) an adhesive handle is attached and pulled to initiate a spalling fracture, and (c) III-V layers are epitaxially grown via HVPE on a Ni-etched spalled Ge substrate

lattice-matched to the substrate, optimum epitaxial growth depends on a high-quality surface. Therefore, the first step was to deposit a nickel stressor layer on a pristine Ge substrate at conditions optimized to produce a fractured surface with minimal defects, as shown in Figure 1.3(a). Then, spalling was mechanically initiated by applying an upward force on a flexible handle adhered to the Ni film, as shown in Figure 1.3(b). Optimizing plating conditions and providing high-quality spalled materials were the primary tasks of this work. Chapter 3 elaborates on fractography techniques used to determine surface quality of spalled Ge substrates.

For III-V cells to be cost competitive, high-speed epitaxial deposition must be incorporated with substrate reuse. Reductions in epitaxial deposition costs in conjunction with 10 reuse cycles could further reduce solar cell price from $37 to $18. [20] Conventional growth techniques such as MOVPE are too expensive to be cost-competitive in one-sun or low-concentration applications, primarily due to the high costs of the metalorganic precursors and the low growth rates. [26] Hydride vapor phase epitaxy (HVPE) is a high-quality growth technique that is significantly faster (up to 300µm/h) and less expensive than MOVPE because it uses elemental metals rather than

expensive metalorganic precursors. [26] NREL recently built a custom HVPE growth system designed to deposit high-quality III-V materials and used it to produce high-quality GaAs junctions via HVPE with performance on par with other growth technologies. [27] For this study, an GaInAsP device was grown on spalled-Ge by NREL, see Figure 1.3(c), and an equivalent structure was grown on a pristine Ge substrate as a control. The spalled substrate GaInAsP solar cell and conventionally processed cell were compared on the basis of standard photovoltaic metrics (FF, efficiency, $V_{oc}$, $J_{sc}$). This work to develop low-cost high-performance solar devices is detailed in Chapter 3 of this dissertation.

## 1.3 Thesis Layout

The technological limitations to remove thin devices from Ge wafers and subsequently reuse the substrates serve as motivation for this thesis. The goal of this work is to use controlled spalling to remove thin films from (100)-Ge substrates using electroplated films. Exhibiting control over a wide spall depth range to minimize material consumption, demonstrating a critical step towards wafer reuse for photovoltaic applications, and addressing fracture behavior during spalling are components this work contributes to the field of controlled spalling.

Chapter 2 is a journal article on which I am first author ready to be submitted to Thin Solid Films. This chapter outlines processing conditions developed to achieve a controlled spalling lift-off for (100)-Ge utilizing three different electrolyte chemistries. Theoretical models were implemented to correlate critical parameters, such as stress and film thickness, to measured spall depth for controlled spalling. Finally, the relationship between stressor layer thickness (1.6-62.6μm), residual tensile stress within deposited films (90-2000 MPa), and subsequent spall depth ranges (0.3-75.6μm) is discussed.

Chapter 3 is an extended abstract which has been accepted to the 2017 IEEE Photovoltaic Specialists Conference as an oral presentation for which I am second author. This chapter presents GaAs films deposited on spalled-Ge followed a single-crystal nature without additional surface processing of the substrate. The first III-V device epitaxially grown on spalled-Ge is demonstrated and the performance is compared to a III-V solar cell grown on a co-loaded bulk Ge substrate.

Chapter 4 is a preliminary summary of fractography of spalled (100)-Ge which provides direction for future improvements to the spalling method utilized in this study. The contributing factors to macro-scale surface roughness of a spalled area are analyzed. Fractography analysis of two distinct regions within the spalled area reveal the formation of arrest lines, river line patterns, and twist hackle. Finally, Chapter 4 discusses the mixed mode loading conditions present during the spalling process which led to imperfect cleavage.

Chapter 5 summarizes the thesis and its contributions to the field of controlled spalling. This chapter develops the technological implications controlled spalling may have on the fields of flexible electronics, particularly for the PV industry. This chapter also mentions modifications which may prevent undesirable topographical features from generating on fractured surfaces.

# CHAPTER 2 EFFECTS OF ELECTROPLATING BATH CHEMISTRY ON CONTROLLED SPALLING IN (100)-ORIENTED GE SUBSTRATES

This chapter presents the findings of electroplating conditions appropriate for controlled spalling and compares experimental film thickness and stress measurements to theoretical spontaneous fracture models. The scientific advancements presented below are ready to be submitted to the journal, "Thin Solid Films." The chapter begins with an overview of the authors' contributions with corresponding supplemental material. This final manuscript was authored by myself (primary author) and co-authored by John Simon (National Renewable Energy Laboratory, Golden, CO), Kevin Schulte (National Renewable Energy Laboratory, Golden, CO), Aaron J. Ptak (National Renewable Energy Laboratory, Golden, CO), and Corinne E. Packard (Colorado School of Mines, Golden, CO).

## 2.1 Author Contributions

In this research, (100)-oriented Ge wafers from AXT, Inc. were provided by Aaron Ptak. I designed an ABS 3D-printed electroplating jig used to electroplate the substrates in front-contact. The relevant CAD drawings for this device are presented in Appendix A. I developed an electroplating set-up and experimentally determined appropriate conditions to achieve controlled spalling. I modified Dr. Cassi Sweet's spalling ramp to prevent wafer breakage and improve test repeatability. I cross-sectioned the spalled films and characterized them using microscopy equipment at the Colorado School of Mines. John Simon and Kevin Schulte developed a method to measure curvature of an electroplated Ge-substrate using XRD at the National Renewable Energy Laboratory. I processed the raw data to calculate residual stress using the Stoney formula. I modified Dr. Cassi Sweet's Mathematica files to describe spalling behavior in Ge based on Suo

& Hutchinson's models for bilayer spontaneous fracture, see annotations and code in Appendix B. After completion of the research, I drafted a manuscript of the findings titled "Effects of Electroplating Bath Chemistry on Controlled Spalling in (100)-Oriented Ge Substrates", and all of the co-authors provided detailed feedback.

## 2.2 Manuscript - Abstract

High-speed electroplating and DC magnetron sputtering have been previously utilized to remove semiconductor devices of various thicknesses from brittle, single-crystal substrates using controlled spalling. However, wide control over spall depth range is limited by the ability to appropriately tune tensile stress within a deposited film. This work investigates the effect of tuning both electroplating current density and electrolyte chemistry on the residual stress and on the achievable spall depth range. Nickel electroplating conditions appropriate for controlled exfoliation of single-crystal germanium films are mapped out for three bath chemistries, each containing different concentrations of phosphorous acid. As phosphorous concentration increased, the electrodeposition current density and plating time required for controlled spalling was substantially reduced. Residual stress within the deposited film increased from 90 to 2000 MPa as phosphorous content increased from 0 to 10mM. We applied linear elastic fracture mechanics to model the bilayer system's spontaneous spalling behavior, which was in agreement with experimental stress measurements. Spall depth generally decreased with increasing internal stress within the deposited film. For the first time, we demonstrate wide control over spall depth within Ge substrates from sub-micron to ~76µm-thicknesses, driven primarily by tailoring residual stress through bath chemistry and plating current density adjustments.

## 2.3 Manuscript - Introduction

Exfoliating devices from substrates offers a path to drastically reduce large-area semiconductor device costs. For example, the high material cost of single-use germanium (Ge) and gallium arsenide (GaAs) substrates has hindered widespread use of III-V photovoltaic (PV) devices in terrestrial applications. Substrate reuse enabled by device exfoliation has been identified as one of the only plausible paths forward for widespread III-V adoption for one-sun and low-concentration PV applications. [20] Bedell *et al.* utilized DC magnetron sputtering and controlled spalling to demonstrate lift-off of single-junction III–V PV devices from a Ge substrate. [28] In that study, exfoliation was achieved by sputtering a tensile Ni film (6μm) on the layers and inducing fracture at a depth of 17μm into the substrate. Bedell *et al.* also noted the magnitude of tensile stress within the deposited film influenced the subsequent spall depth in a manner similar to relationships derived for spontaneous spalling. [13], [29] By adjusting sputtering pressure from a few mTorr to tens of mTorr, the stress could be tuned between 300-550 MPa to attain 7-60μm spall depths in Ge. However, this lift-off method has limited application because it requires expensive sputtering equipment and the deposition process takes many hours. This sputtering technique has also been used to successfully exfoliate flexible devices, such as CMOS circuits removed from silicon substrates and dual-junction InGaP/(In)GaAs tandem solar cells lifted from (100)-oriented Ge. [30]–[32] However, the inability to achieve sub-7μm spall depths resulted in excessive substrate consumption which reduces the number of potential wafer reuses. For widespread application of this technology, a fast and inexpensive lift-off method is needed which allows spall depth control over a wide range. Controlled spalling via electrodeposition is a versatile exfoliation method which can be easily integrated into fabrication lines, extended to any brittle material, and the entire process requires less than 5 minutes. Furthermore, this technique can

achieve fine depth control at room temperature without vacuum or use of hazardous acids.

Controlled spalling utilizes fracture mechanics and application of mechanical force to create wafer cleavage parallel to the surface of a substrate at a precise depth. In this study, an electroplated metal stressor film is utilized to generate a strain mismatch between the deposited layer and the substrate. According to Suo & Hutchinson's models for spontaneous fracture of bilayer systems, spontaneous spalling occurs when the strain mismatch generates a sufficient energy release rate ($G$) to surpass the substrate's critical energy release rate ($G_c$). [13], [33] The current study refers to spontaneous spalling as Ni/Ge film delamination prior to application of mechanical force. Controlled spalling occurs when strain mismatch conditions close to spontaneous spalling allow for mechanical initiation e a crack and controlled propagation of that crack to exfoliate the substrate. [34] The energy release rate ($G$) within the bilayer system is directly proportional to the product of the stressor layer thickness ($h_f$) and square of the tensile stress within the film ($\sigma_f$): [35]

$$G \propto \sigma_f^2 h_f; \tag{2.1}$$

therefore, controlled spalling is achieved by finding the appropriate combination of stressor layer thickness and residual stress within the film. Previous work showed that at controlled spalling conditions, spall depth scales with thickness of the stressor layer, which suggests spall depth can be minimized by reducing the thickness of the deposited film. [16], [18] According to Equation 2.1, any reduction to the film thickness requires increasing the residual stress of the film to maintain controlled spalling conditions. Thus, a method to induce stress exceeding 550 MPa is necessary to achieve spalled depths lower than that achieved via sputtering.

Previous work showed that stress within electrodeposited films can be increased by

adjusting current density or by changing the chemistry of the electroplating solution. One investigation revealed residual stress within electrodeposited Ni linearly increased from 0 to 250 MPa over a range of 0-30 mA/cm$^2$. [36] Sweet *et al.* exploited this behavior to exfoliate 8.1-21.5µm films and III-V layers from (100)-GaAs substrates. [15], [16] In that study, current density was adjusted 30-110 mA/cm$^2$ to produce stresses 280-560 MPa using an all-chloride Watts Nickel bath. This work found extremely high current densities generate stressor layers that are prone to microcracking and tearing, thus further increases to current density above 110 mA/cm$^2$ are not viable. A few studies have shown electrolyte chemistry can be tailored to induce substantial residual stress within films deposited at low current density. Using a 0.6M $Ni^{2+}$ chemistry as a reference, Kwon *et al.* revealed increasing $P^{3+}$ ion concentration from 0 to 10mM increased the electroplated film's internal stress by an additional 178 MPa while holding current density constant at 10 mA/cm$^2$. [35] There are no studies on the effect of tuning both chemistry and plating current density on the achievable spall depth range within Ge substrates.

In this study, controlled spalling via electrodeposition was achieved in a matter of minutes for Ni films a few microns in thickness and in less than 40 min for deposits ~45µm-thick, which is substantially faster than sputtering-based techniques. The effect of electrodeposition bath chemistry on residual stress within the deposited Ni layer and subsequent spall depth was characterized for the Ni/Ge bilayer system. In this study, Ni and Ni–P films were electrodeposited onto Ge substrates using three electrolyte chemistries: Watts Nickel, 5mM phosphorous-based solution, and a 10mM phosphorous-based solution. The Watts Nickel solution was used as a reference to study the effect of phosphorous incorporation into the bath chemistry. Suo and Hutchinson's quantitative spontaneous spalling mechanics models for bilayer systems were utilized to compare experimentally measured stress and spall depths to theory. [13], [14], [33] We

demonstrate a wide range of residual stresses (90-2000 MPa) and Ge spall depths (0.3-75.6µm) by adjustment of a combination of bath chemistry, stressor layer thickness, and current density.

## 2.4 Manuscript – Experimental Methods

(100)-orientated Ge substrates (p-type, 6° offcut towards {111}) approximately 350µm thick were cleaned and prepared by etching for one minute in $NH_4OH$ (BDH, ACS Grade), $H_2O_2$ (Macron Fine Chemicals, 30% Sol.), and deionized $H_2O$ with a volumetric ratio of 2:1:10, respectively. Current-controlled electrodeposition using a nickel anode was performed on 20-mm x 20-mm substrates with a 1.5mm-wide masked exclusion zone around the sample perimeter. Three bath chemistries balanced with deionized water were tested: (1) a Watts Nickel solution consisting of 1.26 M nickel chloride hexahydrate ($NiCl_2{\cdot}6H_2O$, Sigma-Aldrich, 98%) and 0.57 M Boric Acid ($H_3BO_3$, Sigma-Aldrich, 99.5%), (2) a phosphorous-containing solution consisting of 0.6 M $NiCl_2{\cdot}6H_2O$ and 10.0mM phosphorous acid ($H_3PO_3$, Sigma-Aldrich, 99%), and (3) a reduced-phosphorous-content solution consisting of 0.6 M $NiCl_2{\cdot}6H_2O$ and 5.0mM $H_3PO_3$. Each bath was heated to 60ºC with continuous filtration and agitation applied during deposition. For each chemistry, substrates were electroplated at varying current densities and plating times to generate a tensile nickel stressor layer of critical thickness to cause spontaneous spalling. Once spontaneous spalling occurred, the plating time at each current density was reduced until controlled spalling was achieved and then further reduced until residual stress was not sufficient to attain spalling. Following electroplating, each sample was etched in the 2:1:10 solution for three minutes as it was shown to improve spalling reproducibility. The sample was fixed on a compliant rubber strip, and a flexible handle was pre-adhered to the plated region. Controlled spalling was mechanically initiated at 1.05 m/s using a roller set up similar to previous work that studied the controlled spalling of GaAs substrates. [15], [16] For the Watts Nickel, spalled Ge/Ni films were

mounted, cross sectioned, polished, and thicknesses were measured on a LECO Olympus PMG3 optical microscope. For the two baths containing phosphorous acid, the center of each spalled Ge/Ni film was ion beam cross-sectioned using an JEOL IB-0910CP and film thicknesses were measured from scanning electron micrographs (FEI Quanta 600i) across a 1-mm cross section.

Two sample series were used to determine the Young's modulus of deposited films and to estimate the residual stress generated by the stressor layer. In the first series, five 20μm-thick Ni films from each bath chemistry were electroplated on copper substrates. The samples were cross-sectioned and polished using a 3μm-diamond colloidal suspension as a final step. Nanoindentation was conducted on the Ni cross-sections with a Hysitron TI 950 TriboIndenter using a Berkovich tip and 1-dimensional transducer at a loading and unloading rate of 0.4 mN/s. Ten indentations per sample were completed and the reduced indentation modulus measurements were converted to Young's modulus assuming Poisson's ratio of 0.31 for the nickel. [37] To measure the residual biaxial stress in the Ni film, a second series of Ge substrates were electroplated at various current densities and their associated plating time for controlled spalling. The tensile strain generated by the stressor layer caused a slight curvature in the Ge substrate. X-ray diffraction (XRD) was used at 500μm intervals on the backside of electroplated single crystal wafers to measure peak shift in the Ge resulting from the curvature. Using trigonometric principles, the translational displacement and peak shift were used to calculate the substrate curvature. [15] The curvature and Ge/Ni thickness measurements were used to estimate biaxial residual stress within the stressor layer using the Stoney formula. [34], [38] Assuming a Young's modulus of 102.7 GPa for Ge and Poisson's ratio of 0.28, the root-sum-squares method was used to statistically estimate error derived from variations in Ni thickness, curvature, and Young's modulus measurements.

## 2.5 Manuscript – Results and Discussion

We systematically investigated the electrodeposition conditions to achieve controlled spalling and optimal spalled surface quality. At each applied current density, the plating time was adjusted to map out regions where spontaneous spalling, controlled spalling, and no spalling occurred. The data presented in Figure 2.1 provide experimental processing conditions mapping out the appropriate combination of applied current density and deposition time required for controlled spalling using each bath chemistry. The solid colored trendlines fit to the controlled spalling data closely followed an inverse power law, which agree well with a similar power law nature experimentally determined for controlled spalling conditions of electroplated GaAs substrates. [17] For each chemistry, the controlled spalling region was enveloped by a high stress spontaneous spalling region above the curve for each chemistry and by a low stress non-spalling region below the curve. For instance, substrates plated longer than 6.25 min in Watts Nickel at 110 $mA/cm^2$ accumulated too much stress and consistently spontaneously spalled. When plating time was reduced to less than 4.25 min, the stress and thickness combination fell into a sub-critical region wherein spalling was not achievable at all. At this specific current density, the optimum controlled spalling conditions occurred in a two-minute window (4.25-6.25 min). For comparison, Sweet *et al.* determined controlled spalling conditions for GaAs at 110 $mA/cm^2$ and 3.5 min were similarly bounded by spontaneous spalling and sub-critical regions. Bedell *et al.* also found the appropriate combinations of residual stress and Ni thickness for controlled spalling in sputtered Ge wafers were bounded by these regions, but did not specify exact processing conditions. [18]

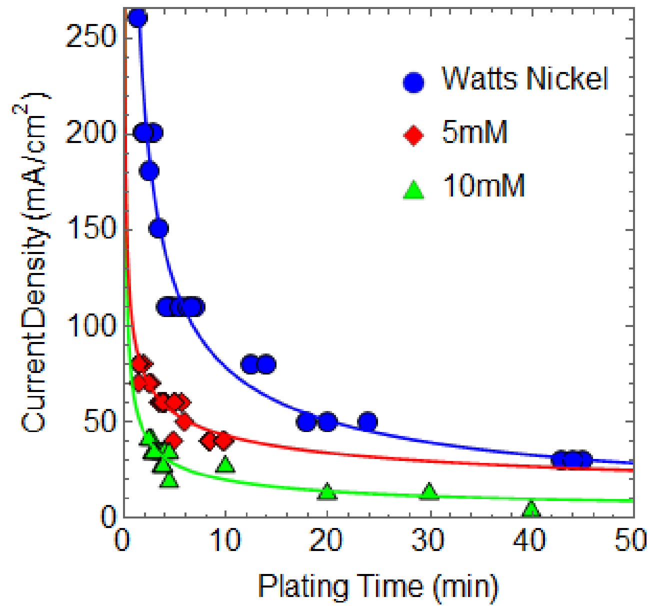


Figure 2.1: Controlled spalling conditions for Watts Nickel, 5mM $H_3PO_3$, and 10mM $H_3PO_3$ bath chemistries emphasized with fitted trend lines

The overall range of plating times and current densities to achieve controlled spalling narrowed as phosphorous content increased. This effect is best exemplified by comparing the current densities required to achieve controlled spalling at plating times ~2.0 min for each chemistry. For the Watts Nickel solution, the current density to attain spalling in that plating time range occurred at 260 mA/cm$^2$ and required a relatively thick stressor layer (11.1µm). Increasing the phosphorous concentration to 5mM dropped the appropriate current density to 80 mA/cm$^2$ while and reduced the critical stressor layer to 1.8µm. Doubling the phosphorous concentration to 10mM reduced the spalling current density by nearly half to 42 mA/cm$^2$. Because tuning current density is typically the driver to control residual stress, Equation 2.1 suggests at lower current densities the critical stressor layer thicknesses is expected to significantly increase in order to maintain the necessary energy release rate for controlled spalling. However, both critical current density and stressor layer thickness decreased for samples electroplated in the phosphorous-containing baths relative to Watts Nickel. Therefore, if Equation 2.1 holds true, adding

phosphorous must have the effect of inducing additional stress.

Edge effects and parallel striations were observed on control-spalled substrates and the matching exfoliated Ni/Ge film. Figure 2.2 shows a top-view optical image of a representative spalled-Ge substrate with the spalled-Ge side of the exfoliated film exposed. Edge effects were

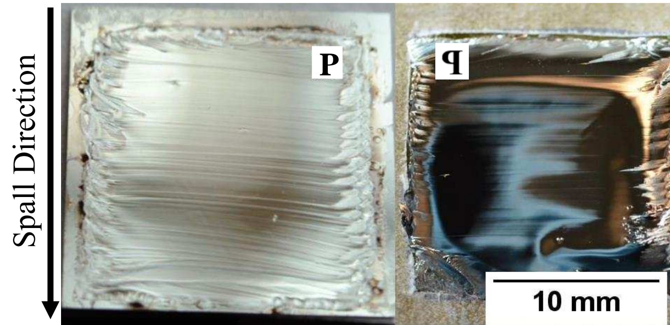


Figure 2.2: (left) Ge substrate with a 1.5mm exclusion zone following controlled spalling and (right) its associated exfoliated Ge/Ni film with the Ge side exposed. Letter ‘P’ represents the orientation and alignment of features at matching areas of the substrate and film

observed to extend approximately 2-mm inward along the inside perimeter of both the substrate and the Ge film. These features were identified as river line patterns via SEM and their origin has been attributed to a shear-component stress ($K_{III}$) acting perpendicular to the fracture direction. [39] Features parallel to the fracture front were also found to extend across the spalled area and were aligned perpendicular to the spalling direction (direction in which the crack propagated). These well-defined lines are thought to be arrest lines produced when the crack comes to a halt, before resuming its propagation as a result of the rolling process. [28], [40] Neither river line patterns nor arrest lines are dependent on crystallography of the (100)-Ge wafers. This was determined by performing controlled exfoliations along different crystallographic directions where the striations always followed the spall propagation direction and not any particular crystallographic direction. At the center of each spalled area, fracture was not affected by these

macroscopic defects. Cross-sectional micrographs of spalled films within this region showed the spalled Ge layer locally followed the (100) cleavage plane, shown in Figure 2.3. Similar cross-sectional micrographs were also used to measure thickness of each layer within the center of spalled films.

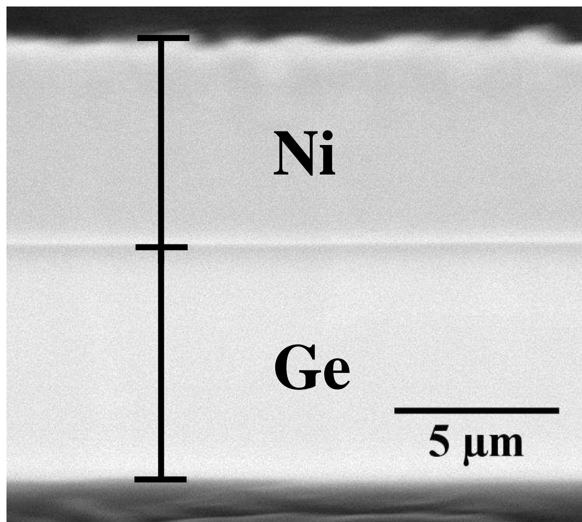


Figure 2.3: SEM micrograph of a cross-sectioned spalled film showing the thickness of spalled Ge and electroplated Ni deposited using the 5mM $H_3PO_3$ chemistry

The spall depths and critical stressor layer thickness were measured for each chemistry and compared to Suo and Hutchinson's spontaneous spalling mechanics. The measurements summarized in Table 2.1 show the phosphorous-based chemistries drastically minimized spall depth compared to Watts Nickel even though critical current density ranges overlapped. Between all chemistries, the accessible spall depth range of 0.3-75.6µm shows controlled spalling via electrodeposition is a promising method to exfoliate flexible electronics devices with minimal substrate consumption. Each data point contributed to the aggregate series in Table 2.1 (see page 21) are plotted on Figure 2.4 (see page 22), with each data point representing one sample. The 5mM chemistry resulted in the lowest spall depth range (0.3-15.1µm) and highest spalled surface quality. For the 10mM chemistry, however, large spall depth variability at stressor thicknesses of

2-3μm produced unviable surface morphology. Compared to the 5mM chemistry, Figure 2.4(b) shows the 10mM chemistry required thicker stressor layers to produce spalls of equivalent thickness. The behavior could be explained by observing granular spalling or film microcracking for 10mM samples deposited at current densities above 28 mA/cm$^2$. Figure 2.5 shows a Ge substrate following controlled spalling during which the initially continuous Ni film delaminated into granular and discontinuous Ge/Ni segments. Edge effects emerged within each segmented region due to competing fracture modes which led to unexpectedly deep spalls. Kwon *et al.* discovered similar micro-cracking in Ni-P films deposited at 20 mA/cm$^2$ on Si wafers and attributed the behavior to massive increases in stress resulting from increased phosphorous concentration within the deposited film. [35]

Table 2.1: Measured Ni film thicknesses and Ge spall depth for control-spalled samples at various current densities

| | Current Density (mA/cm$^2$) | Stressor Film Thickness (μm) | Spall Depth (μm) |
|---|---|---|---|
| Watts Nickel | 30-260 | 11.1-62.6 | 29.5-75.6 |
| 5mM | 40-80 | 1.6-6.8 | 0.32-15.1 |
| 10mM | 28-42 | 1.8-8.6 | 1.0-21.5 |

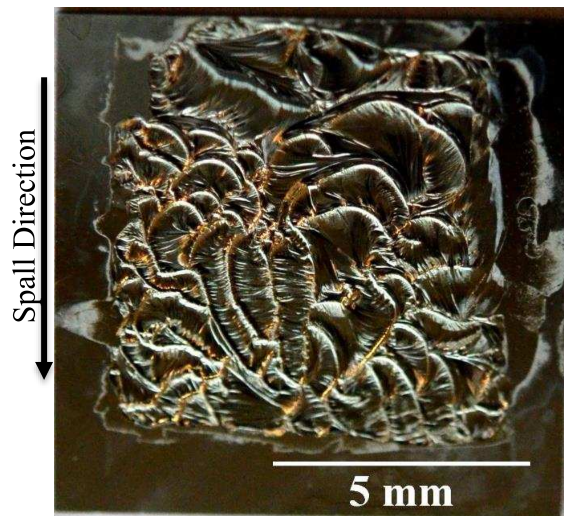


Figure 2.5: A Ge substrate electroplated in 10mM chemistry after granular spalling

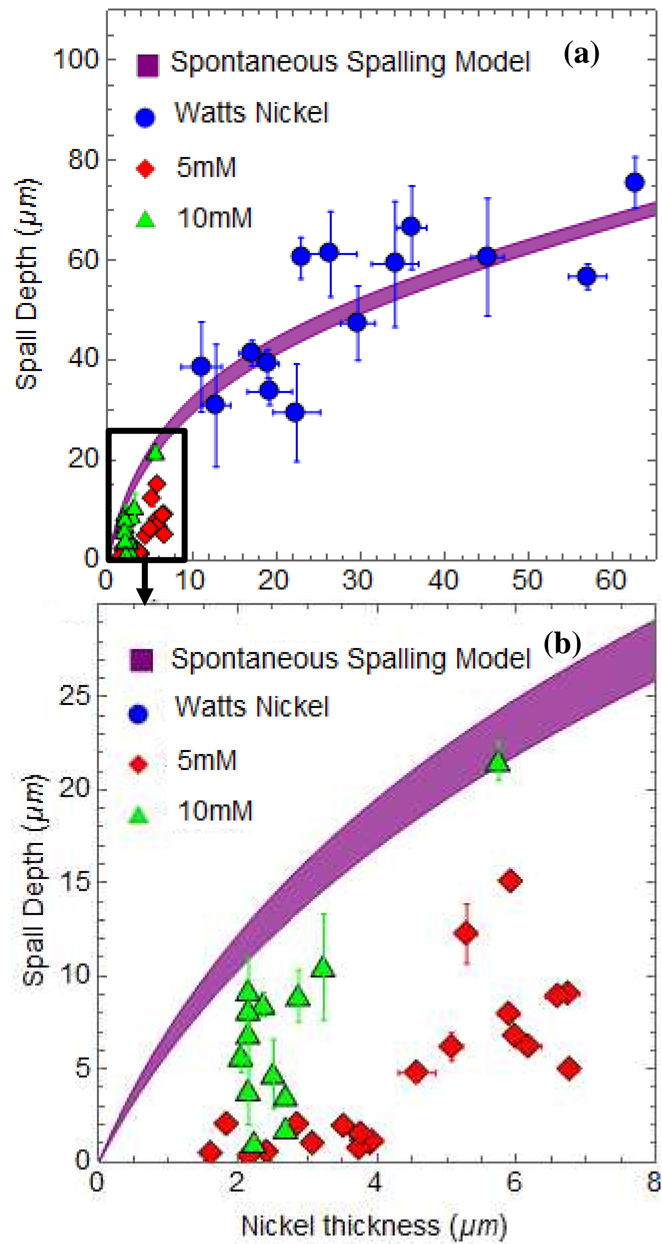


Figure 2.4: (a) Theoretical and experimental Ge spall depth as a function of stressor layer thickness for each bath chemistry (b) The phosphorous based chemistries significantly reduced spall depths

To compare experimental measurements against theory, we used Suo and Hutchinson's full-solution model for spontaneous bilayer fracture to approximate the spall depth of (100)-oriented Ge as a function of stressor layer thickness. [13], [16] The model was modified using measurements and assumptions specific to the Ni/Ge bilayer system. First, substrate thickness was assumed a constant 350µm since the model was found insensitive to variations up to ±20µm. The magnitude of elastic anisotropy relative to isotropic cubic single-crystals as defined by the anisotropic factor is low for Ge (A* = 2.7) and nearly identical to that of silicon. [41] Although Ge is weakly anisotropic, the model is based on linear elastic fracture mechanics and assumes isotropic mechanical properties during fracture. The model also utilizes a parameter, ω, that is nearly invariant over wide ranges of elastic dissimilarity between the two materials, steady-state crack depth, and substrate thickness variables and therefore, held at a constant value of 52°. [13], [42] While an ideal Young's modulus for bulk Ge (102.7 GPa) could be assumed for the substrate, the Young's modulus for electroplated Ni can vary. [36] Nanoindentation revealed no statistically significant difference between the Ni films plated with each chemistry; the average of all measurements and standard deviation (221±20 GPa) was used in the model. Figure 2.4(a) shows both experimental thickness measurements and the theoretical spall depth trend from the bilayer model. The width of the theoretical curve reflects the uncertainty in the averaged elastic modulus for the stressor layer. The Watts Nickel samples loosely followed the model's non-linear trend over a wide spread range of Ni thicknesses. However, spall depth increased more gradually than predicted for the 10mM samples and granular spalling in the 5mM samples limited any discernment of a trend. To determine why the 5mM and 10mM chemistries resulted in substantially smaller spall depths relative to Watts Nickel, residual stress within the Ni film was measured.

Experimental stress measurements revealed tailoring bath chemistry can induce

substantially more residual stress within the Ni layer than can be achieved by tuning electroplating current density. Figure 2.6 shows the stress measurements from the samples electroplated under the same current densities as those presented in Table 2.1. The stress error bars were derived from measurement errors in substrate thickness, stressor layer thickness, and sample curvature. Using previously stated assumptions and the measured Ni modulus, Suo and Hutchinson's models were utilized to approximate the spontaneous spalling behavior of (100)-oriented Ge. The solid line in Figure 2.6 represents the combinations of residual stress and stressor layer thicknesses that define the lower bound of the theoretical spontaneous spalling envelope (purple-shaded region). In this figure, nearly all samples plated under conditions appropriate for controlled spalling are located in the stable region below the spontaneous envelope. The experimental results followed an inverted power law trend, and for each chemistry measured stress generally increased with applied current density. The Watts Nickel solution produced relatively low stresses (90-530 MPa) over a large current density range of 30-260 mA/cm$^2$, which required comparatively thick stressor layers to

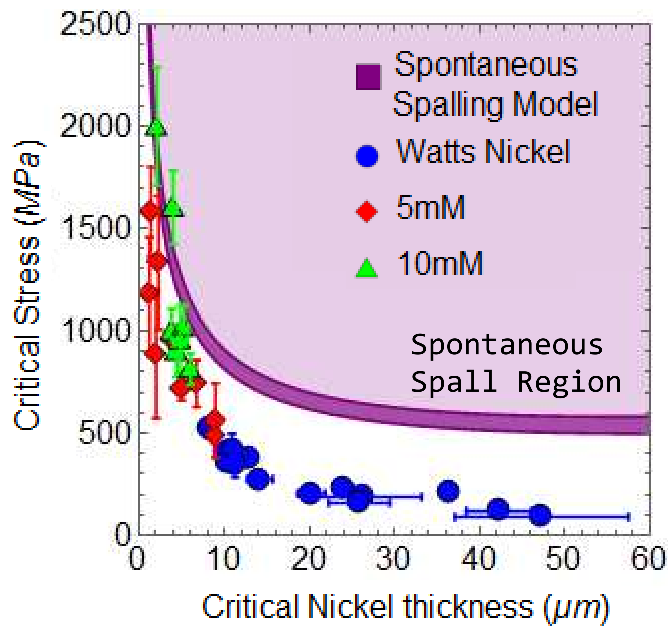


Figure 2.6: Stress measurements for each chemistry plated under controlled spalling conditions. Increasing phosphorous content drastically increases residual tension.

achieve the energy release rate appropriate for controlled spalling per Equation 2.1. Applying 40-80 mA/cm$^2$, the 5mM electrolyte chemistry produced residual stresses of 490-1580 MPa. Higher stresses (810-2000 MPa) were measured for 10mM samples electroplated using 28-42 mA/cm$^2$. For the 10mM bath, granular spalling and spontaneous spalling observed at low current densities were indicative the phosphorous content had a significant effect on the Ni film during deposition.

One plausible explanation the 5mM and 10mM chemistries produced higher stress levels than Watts Nickel can be explained by prior literature on the effect of phosphorous incorporation within the deposited stressor layer. Metallographic characterization of the deposited Ni films was not performed in this study, but several studies have confirmed phosphorous segregates to the grain boundaries during electrodeposition and produce nanocrystalline grains at low current densities. [43], [44] TEM observations on as-deposited Ni-P alloys showed phosphorous ions cause severe lattice distortions and defects at the grain boundaries. As phosphorous content in the deposit is increased, a crystalline to amorphous transition proceeds via gradual decrease in grain size and increase in lattice distortion. [44], [45] For this study, we expect lattice distortion from grain boundary segregation accumulation of residual stress in the film, exceeding that attained by tailoring electroplating current density or sputtering pressure. Therefore, we show that tuning bath chemistry serves as an effective method to achieve wider control over of the desired stress states (90-2000 MPa) and spall depth (0.3-75.6μm) than any processing technique previously studied and can do so in dramatically less time than sputtering. The 5mM $H_3PO_3$ chemistry was found to be optimal for sub-10μm applications while the Watts Nickel is suggested for thicker spall depths. Adoption of the 10mM chemistry requires further optimization to prevent film microcracking during spalling.

## 2.6 Manuscript - Conclusion

In this study, (100)-oriented Ge substrates were prepared for spalling by electrodepositing a highly-stressed nickel layers at varying current densities. The appropriate plating conditions to achieve controlled spalling were investigated for three bath chemistries: Watts Nickel, a solution containing 5mM phosphorous acid, and a 10mM phosphorous acid solution. The controlled spalling conditions for each chemistry were enveloped by spontaneous spalling and sub-critical regions. Increasing phosphorous content substantially reduced the required current density and average critical stressor layer thickness to achieve controlled spalling. For all three chemistries, the measured spall depth generally increased with thicker stressor layer thicknesses. Linear elastic spontaneous spalling models correlated well with cross-section measurements of spalled Ni/Ge films electroplated in the Watts Nickel solution. By tuning bath chemistry, we show a path to control spall depth over a range of <1µm to >75µm into single crystal (100)-oriented Ge, providing exfoliated Ge films for a variety of applications. Increasing electroplating bath phosphorous content drastically increased stress in the deposited Ni layer, allowing stresses up to 2000 MPa to be achieved. We showed that tailoring bath chemistry and current density levels is a reliable method to tune stress and achieve a wide spall depth range in (100)-Ge.

# CHAPTER 3 III-V SOLAR CELLS GROWN ON REUSABLE GE SUBSTRATE

Reproduced with permission from IEEE 44th Photovoltaic Specialists Conference and the co-authors listed below. Copyright 2017 IEEE Journal of Photovoltaics

This chapter demonstrates spalled Ge substrates can be used as a platform to epitaxially grow single crystal GaAs films and GaInAsP solar cells with equivalent performance to conventionally processed GaInAsP cells. The results presented below are from an extended abstract accepted as an oral presentation for the 2017 IEEE Photovoltaic Specialists Conference. The chapter begins with an overview of the authors' contributions with corresponding supplemental material. This abstract was authored by Nikhil Jain (National Renewable Energy Laboratory, Golden, CO) and co-authored by myself, John Simon (National Renewable Energy Laboratory, Golden, CO), Steve Johnston (National Renewable Energy Laboratory, Golden, CO), Sebastian Siol (National Renewable Energy Laboratory, Golden, CO), Kevin Schulte (National Renewable Energy Laboratory, Golden, CO), Corinne E. Packard (Colorado School of Mines, Golden, CO), David Young (National Renewable Energy Laboratory, Golden, CO), and Aaron J. Ptak (National Renewable Energy Laboratory, Golden, CO).

## 3.1 Author Contributions

In this chapter, my contributions include examining the quality and roughness of spalled Ge-substrates through the use of atomic force microscopy and white-light digital microscopy. I developed a process to laser scan the substrate and provide macro-scale roughness in the sample center. MATLAB codes I developed and annotated in Appendix C were used measure an average spall depth over an 8-mm x 8-mm area. I used scanning electron microscopy to measure spalled film thickness and show the spalled-Ge's planar nature. Furthermore, I nickel-etched the spalled

Ge substrates and provided them to the primary author, Nikhil Jain. Using the National Renewable Energy Laboratory's hydride vapor phase epitaxy reactor, Nikhil grew GaAs buffer layers and GaInAsP solar cells on spalled and bulk Ge substrates. John, Steve, Kevin, and Sebastian assisted in collecting standard photovoltaic metrics (FF, efficiency, $V_{oc}$, $J_{sc}$). Aaron and Corinne provided conceptual feedback and direction for the project. All authors provided edits of this extended abstract prior to final submission.

### 3.2 Manuscript - Abstract

Substrate reuse offers a promising route towards enabling high-efficiency III-V solar cells to become cost-competitive for one-sun terrestrial applications. Controlled spalling has been demonstrated previously for the successful exfoliation of devices with no degradation in performance, but a critical requirement of substrate reuse is the demonstration of high quality regrowth on previously used substrates. In this study, Ge films were spalled using an electroplated Ni stressor layer, and the fracture surface was characterized. Initial heteroepitaxial GaAs films grown on spalled-Ge substrates by hydride vapor phase epitaxy were found to be nearly conformal and single crystal in nature, despite the lack of any surface preparation. We show the first demonstration of III-V solar cells (GaInAsP, Eg~1.7 eV) growth on spalled-Ge substrate to assess the viability of substrate reuse. We demonstrate equivalent performance for solar cell grown on spalled-Ge and on a co-loaded bulk Ge substrate, despite the residual roughness on the spalled-Ge substrate. This initial demonstration of combining substrate reuse with the ability to grow III-V solar cells at very high growth rate is a promising step towards low-cost III-V photovoltaics.

### 3.3 Manuscript - Introduction

III-V compound semiconductor based solar cells hold world-record efficiencies for both single- and multi-junction solar cells. However, expensive III-V deposition processes and high material cost of substrates (Ge or GaAs) have limited their widespread use in one-sun terrestrial applications [20]. Combining substrate reuse and growth of III-V devices via a low-cost and high-throughput deposition technique, such as hydride vapor phase epitaxy (HVPE) [46], [47], could offer a path to drastically reduce the cell cost.

Controlled spalling is a fast, capable method for substrate removal that does not impact device performance [17], [24]. Spalling occurs when a deposited stressor layer generates a stress field of sufficient energy within the sample to surpass the substrate's fracture toughness [17]. In (100)-oriented Ge, an initiated crack will cleave parallel to the substrate surface at a depth guided by the stress field ahead of the crack front. The depth of the fracture, which can be tuned to minimize substrate consumption, is determined mainly by the thickness of the stressed film. The entire process could be easily integrated into fabrication lines and takes only a few minutes, which are both required for achieving scalability for large volume manufacturing. The spalling approach to wafer reuse is a much higher throughput process than the traditional chemical epitaxial lift-off technique. Though spalling of devices and subsequent reuse of spalled substrates has been demonstrated in GaAs, unfavorable orientation of cleavage planes generates a faceted fracture that consumes a significant thickness of the substrate [17]. Spalling from Ge substrates to avoid a faceted fracture has been successfully demonstrated [24], but none have extended the process to successfully grow III-V devices on a spalled Ge surface.

In this paper, we investigate the topography of spalled (100)-oriented Ge substrates and demonstrate the growth of nearly conformal and single-crystal GaAs films on spalled-Ge substrate

via HVPE. We report the growth of GaInAsP solar cells (Eg~1.7 eV) nominally lattice-matched to the Ge substrate grown at nearly ~0.7 µm/min. The viability of regrowth on a spalled Ge surface was assessed by comparing performance of GaInAsP devices grown on spalled-Ge and on co-loaded epi-ready Ge substrate. Key factors limiting the solar cell performance are identified and pathways for future improvements for substrate reuse are discussed.

## 3.4 Manuscript – Experimental Methods

(100)-orientated Ge substrates (p-type, 6° offcut) were etched for one minute in a $NH_4OH$:$H_2O_2$:$H_2O$ solution with a respective volumetric ratio of 2:1:10. A nickel stressor layer was electroplated on each 19.5-mm x 19.5-mm Ge substrate leaving a 2-mm wide exclusion zone around the sample perimeter. Controlled spalling was initiated using a roller similar to the set up as shown in Figure 3.1(a) (see page 31). The surface quality of spalled-Ge substrates was characterized using a DI-3100 atomic force microscope (AFM), a Keyence VHX-5000 digital microscope, and a Keyence LC-2400 series laser profilometer. The center of the spalled Ge/Ni film was cross-sectioned and analyzed on FEI Quanta 6001 environmental scanning electron microscope (SEM) across a 1-mm cross section. The spalled Ge substrates were cleaned of any residual Ni in Transene TFG etchant and the samples were degreased in acetone/isopropyl alcohol prior to III-V growth.

Initial GaAs nucleation and buffer layers on Ge substrates (both bulk and spalled) were grown at 675°C in a custom HVPE reactor [46], [47]. These films were characterized by X-ray diffraction (XRD) using a Brucker D-8 diffractometer with a Vantec 500 area detector to obtain wide-angle two-theta 2D plots. The GaInAsP solar cell ($E_g$~1.7 eV) structures were grown at 625°C at ~ 0.7µm/min, details of which are reported elsewhere [47]. The device schematic of the heterojunction GaInAsP solar cell is shown in Figure 3.1(b). The quantum efficiency (QE) and

specular reflectance were measured on a custom-built QE set-up, and current density-voltage (JV) measurements were performed on an XT10 solar simulator, tuned to simulate the AM1.5G spectrum at 1000 W/m$^2$. Dark lock-in thermography (DLIT) images were acquired in both forward and reverse bias to investigate localized defects and potential shunts in the solar cells under reverse bias.

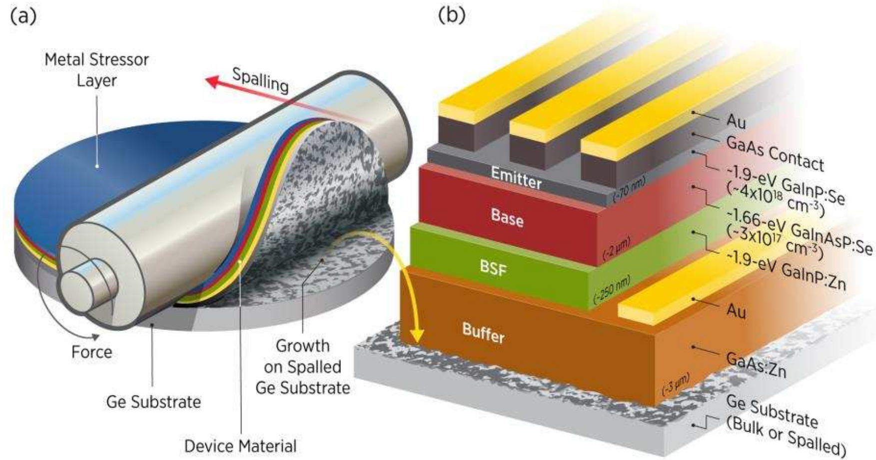


Figure 3.1: (a) Representation of spalling process to remove thin Ge-film from Ge substrate and (b) device schematic of GaInAsP solar cell grown on spalled-Ge substrate

## 3.5 Manuscript – Results and Discussion

### 3.5.1 Controlled Spalling of Ge Thin-Films from Ge Substrate

Due to the high plating rate and bath chemistry, biaxial residual stress within the stressor layer causes tensile stress in the parent substrate. Controlling the deposited Ni thickness, thereby tuning the residual stress field, allows control over subsequent spall depths. Following established electroplating theory; the desired Ni thickness was deposited through controlling the applied current density and plating time. We experimentally determined that a current density of 60 mA/cm$^2$ and plating time of 3.90 min allows for reproducible spall depths. The thicknesses of the spalled-Ge film and the Ni stressor layer ranged between 2-10µm and 3.7-4.0µm, respectively. The spalled-Ge films followed the (100) cleavage plane and the thickness of the Ge film remained

nearly constant across the 1-mm section that was analyzed (see Figure 3.2). Surface features on the spalled Ge film surface corresponded well with the matching area on the spalled substrate. On the spalled-Ge substrate, the edge effects were observed to extend approximately 2-mm along the inside perimeter, as shown in Figure 3.3(a) (see page 32). AFM scans measured an RMS roughness ($R_q$) of 2.3nm over a 25-µm x 25-µm area in the sample center, as shown in Figure 3.3(b). However, larger area scans obtained by laser profilometry showed an RMS roughness ($R_q$) of 2.14µm over an 8-mm x 8-mm scan area. This macroscale roughness suggests the spalled surfaces are far from perfect and the subsequent epitaxy could be challenging. We plan to spend efforts toward *ex-situ* processing to improve the morphology of the spalled surfaces.

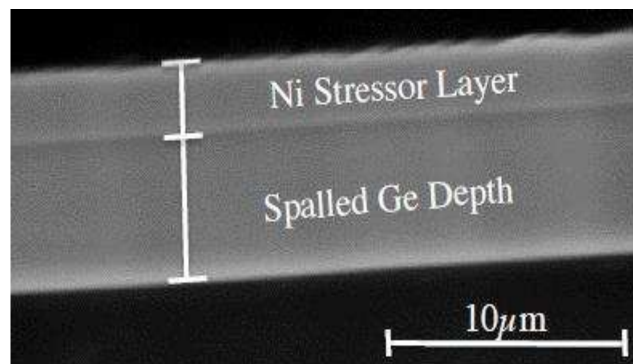


Figure 3.2: Cross-sectional SEM image representative of spalled-Ge film attached to the electroplated Ni stressor layer post-spalling

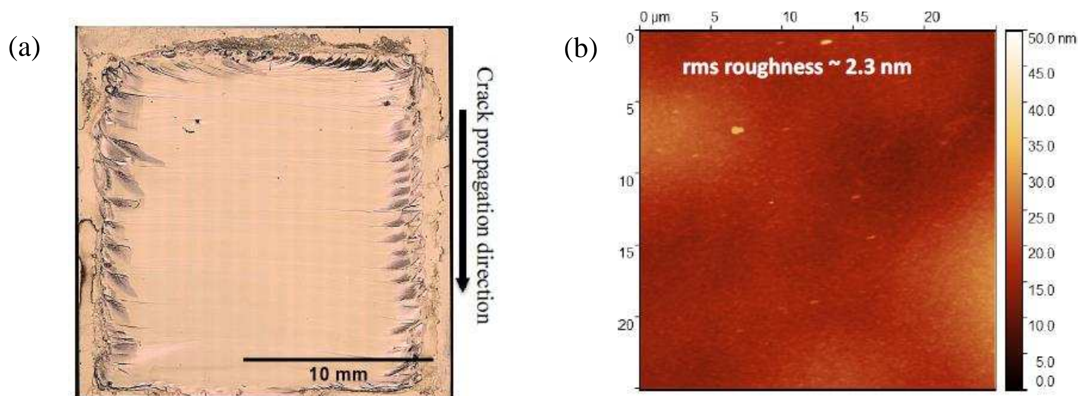


Figure 3.3: (a) Plan-view optical image of spalled Ge substrate with a 2-mm wide exclusion zone along the perimeter and (b) a representative 25µm x 25µm AFM scan in the sample center area.

### 3.5.2 GaInAsP Solar Cell Growth on Spalled-Ge by HVPE

The initial GaAs films grown on spalled-Ge substrates followed the morphology of the starting surface and the growth was nearly conformal. XRD measurements (see Figure 3.4(a)) suggest single crystal GaAs growth was maintained on the spalled-Ge substrate and no additional diffraction peaks were detected for GaAs growth on spalled-Ge in comparison to the control sample (GaAs on bulk Ge sample). Optical microscopy of surface morphology before and after growth of a ~1.5um thick GaAs film are shown in Figure 3.4(b).

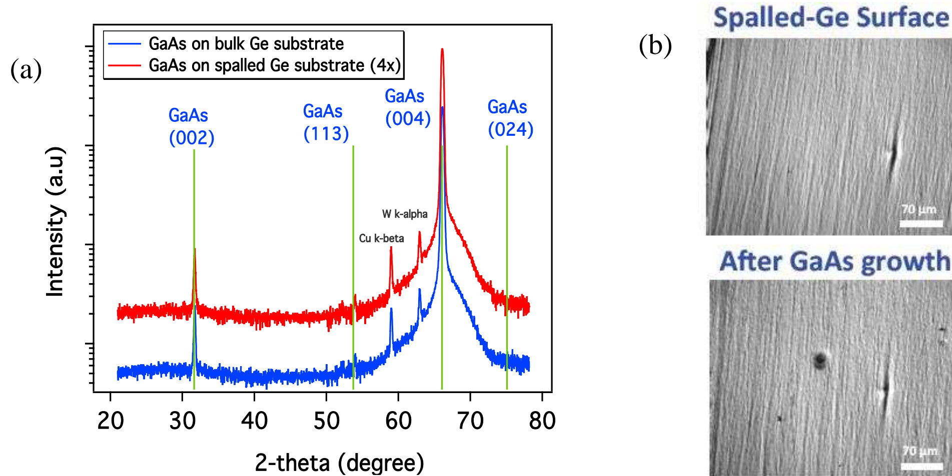


Figure 3.4: (a) Wide-angle 2-theta XRD pattern for GaAs epitaxial films grown on bulk Ge and spalled-Ge substrate suggesting single crystal growth maintained on spalled-Ge, (b) plan-view optical image showing morphology of spalled-Ge substrate before and after ~1.5µm GaAs growth.

The EQE and JV characteristics of GaInAsP solar cells grown on spalled-Ge and on co-loaded bulk Ge substrates are shown in Figure 3.5(a) and (b), respectively (see page 34). Clearly, the performance of the device grown on the bulk Ge substrate requires significant development. However, the equivalent performance (within the error of the measurement error) of the devices grown on the spalled and bulk Ge substrates shows that we have not yet hit any substrate-quality-related limit. This gives promise that as the growth of GaInAsP on bulk Ge is improved, the efficiency of devices on spalled Ge will improve as well. The cell on spalled-Ge showed an open-

circuit voltage ($V_{OC}$) of ~1.00 V, and $J_{SC}$ ~11.5 mA/cm$^2$ with an efficiency of ~7.6%. Performance of GaInAsP cells even on the bulk Ge substrate is far from optimal and does not appear to be intrinsic to growth on spalled-Ge substrates. The DLIT images for these cells (see Figure 3.5(c)) did not reveal any localized defects or heating spots. Modeling using Hovel's drift-diffusion equation suggests that higher dark-current associated with depletion region recombination is responsible for limiting the $V_{OC}$. The heavily doped base layer ($N_A$~3x10$^{17}$ cm$^{-3}$) appears to be responsible for the poor long-wavelength photoresponse, which we attribute to short diffusion length ($L_n$~0.2µm from modeling). The short-wavelength response in these cells is limited by the lack of a passivating window layer.

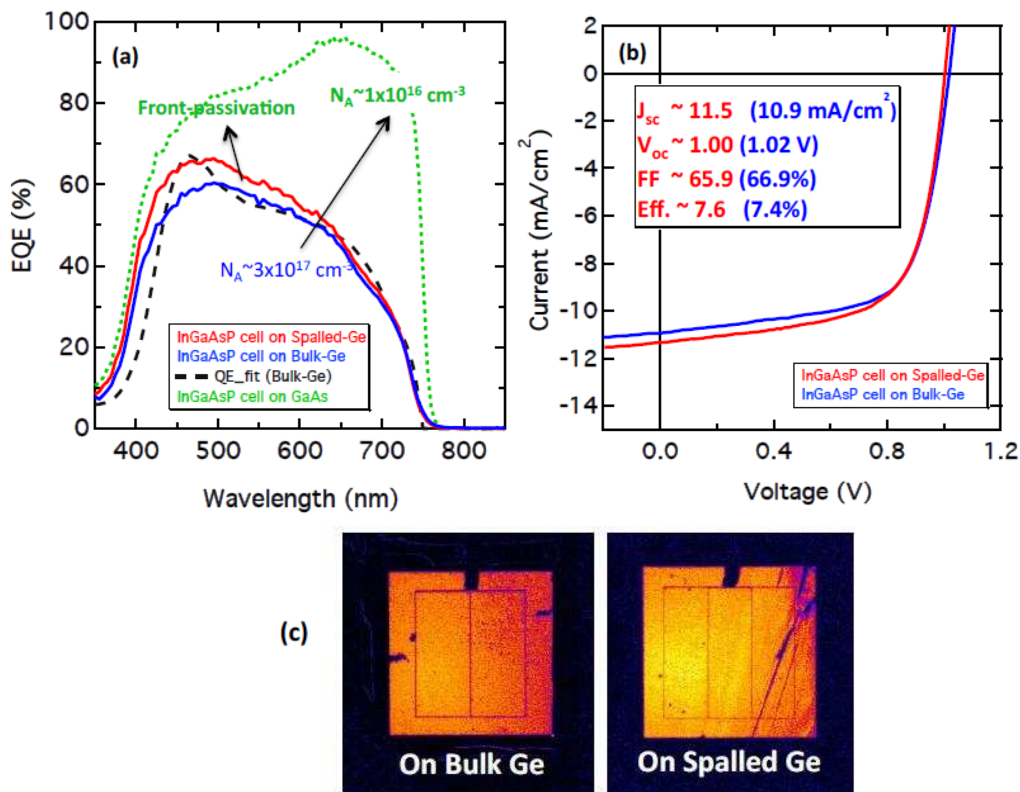


Figure 3.5: (a) EQE and (b) JV characteristic of GaInAsP heterojunction solar cells grown on spalled-Ge (red) and epi-ready bulk Ge substrate (blue) highlighting nearly equivalent performance. An optimized GaInAsP homojunction device with front passivation and lower base doping grown on GaAs is also shown to highlight potential knobs for performance improvement. (c) Dark lock-in thermography images at 1V reverse bias voltage reveal no localized defects or heating spots.

The equivalent performance of prototype GaInAsP cells on spalled and bulk Ge substrate is encouraging; however, significant challenges need to be addressed for viability of substrate reuse via spalling. Future efforts will focus on *ex-situ* surface preparation to improve the morphology of the spalled-Ge surface. While the quality of initial GaAs buffers on bulk and spalled-Ge is promising, the cell growth conditions are far from optimal. Lowering the base doping to improve the carrier collection and incorporating a passivating InGaP window layer are expected to improve the overall performance. Similar GaInAsP solar cell development efforts on GaAs substrates have recently enabled efficiencies as high as 18.7% [47].

### 3.6 Manuscript – Conclusion

We show the first demonstration of III-V solar cells grown on a spalled-Ge substrate as a promising approach toward wafer reuse via controlled spalling. Initial hetero-epitaxial GaAs films grown by hydride vapor phase epitaxy on spalled Ge substrate were nearly conformal and single crystal in nature, despite lack of any additional surface preparation. Prototype GaInAsP solar cells grown on spalled-Ge and co-loaded bulk Ge substrates show nearly equivalent efficiency of ~8% under one-sun. Pathways for future improvements in spalled-Ge surfaces and device performance are identified. This initial demonstration of combining substrate reuse together with the ability to grow III-V solar cells at a very high growth rate by HVPE presents a promising path toward low-cost III-V photovoltaics.

# CHAPTER 4 FRACTURE PATTERNS ON SPALLED (100)-GERMANIUM SURFACES

Macroscale roughness observed on fractured Ge surfaces suggested crack propagation did not follow cleavage along a single {100} plane during the spalling process, which nominally results in a perfectly planar and featureless surface. When applied stresses are not normal to the crack tip, stress fields are modified and increase the stress intensity $K_{II}$ away from zero. Under these conditions, a propagating crack is guided into new cleavage planes and directions, thus deviating from planar behavior and often causing topographical features to arise on the fractured surface. Undesirable features were visually observed on spalled Ge surfaces and the matching exfoliated Ge film. Well-defined striations were also observed across the entire spalled surface. Relatively rough features were constrained along the inside perimeter of the spalled area; those areas are hereafter referred to as edge-affected zones. Since excessive roughness could introduce interfacial defects during large scale epitaxial growth and impede optimal mechanical, optical, and electronic properties, several characterization methods were utilized to determine the stress states during spalling which cause imperfect cleavage. The work presented in this chapter focuses on documenting and understanding the origins of the edge-effect zones, observed parallel striations, and macroscopic curvature of the spalled surface.

Laser scanning, previously mentioned in Chapter 2, was performed on a Keyence LC-2400 series laser profilometer with a ±0.025µm resolution. Stage velocity was set to 5 mm/sec and the spacing between scans was kept a constant 50µm. Approximately 12 million data points were acquired for each scanned 20-mm x 20-mm sample. The files were exported to TrueMap v5.2.16 to generate a 3D model and height map of the fracture substrate and to remove missing data points. Digital white light microscopy was performed on a Keyence VHX-5000 digital microscope using

a VH-Z500R lens with a numerical aperture of 0.82. Stitching was completed using a 0.1μm pitch between images under a sharpening mode lighting condition while utilizing a polarizer. SEM imaging of the spalled substrates was performed at various angles on an FEI Quanta 6001.

The first section in this chapter introduces two distinct regions of spall depth behavior within spalled areas: (1) a region dominated by steady-state fracture and (2) edge-affected zones. In section 4.2, RMS roughness from large-scale curvature of the spalled surface within the steady-state region is compared to progressive undulations observed throughout the spalled area. The parallel striations are confirmed as arrest lines in section 4.3 by SEM characterization and spalling experiments. In section 4.4, the presence of river line patterns and twist hackle within edge-affected zones verify mixed-mode loading is present during spalling. This section further discusses the relation between these distinct topographical features and stress states present during the spalling process. Finally, the key findings and technological impacts of this chapter are summarized in section 4.5.

## 4.1 Macro-scale Fracture Behavior

The overall profile of fractured surfaces was non-planar, which can limit spall depth control over large areas and lead to excessive material consumption. Figure 4.1 shows a color height map of a representative spalled Ge substrate and a line scan of the surface profile. The line scan identifies three distinct regions of interest. The original surface (blue) was used as a reference plane for spall depth measurements. Edge-affected zones (red) were constrained within 2-mm of the spalled area perimeter and included significant spall depth variation. Spall depth behavior typically followed a periodic variation in height within the first few millimeters of the spalled region. Steady-state fracture appeared to dominate away from the edges as the surface began to follow a nearly planar behavior at the at the center of the spalled area. However, both the height

map and the cross-sectional view show spall depth increased radially away from the sample center until edge effects dominated the fracture behavior. Shown in Figure 4.2, additional profile scans of ten samples at the sample center express the typical spall depth variation measured within the steady-state region. Due to the surface's semi-spherical nature, spall depth near the edge of the steady-state region could increase 10μm relative to the depth measured at spalled area center. Furthermore, the non-planar fracture behavior can lead to excessive material consumption near the spalled edges and severely limit the number of potential substrate reuses. Within the spalled area of the color height map in Figure 4.1, parallel striations oriented perpendicular to the spall direction can be observed. These features and macroscopic curvature of the steady-state region can add significant roughness to the fractured surface.

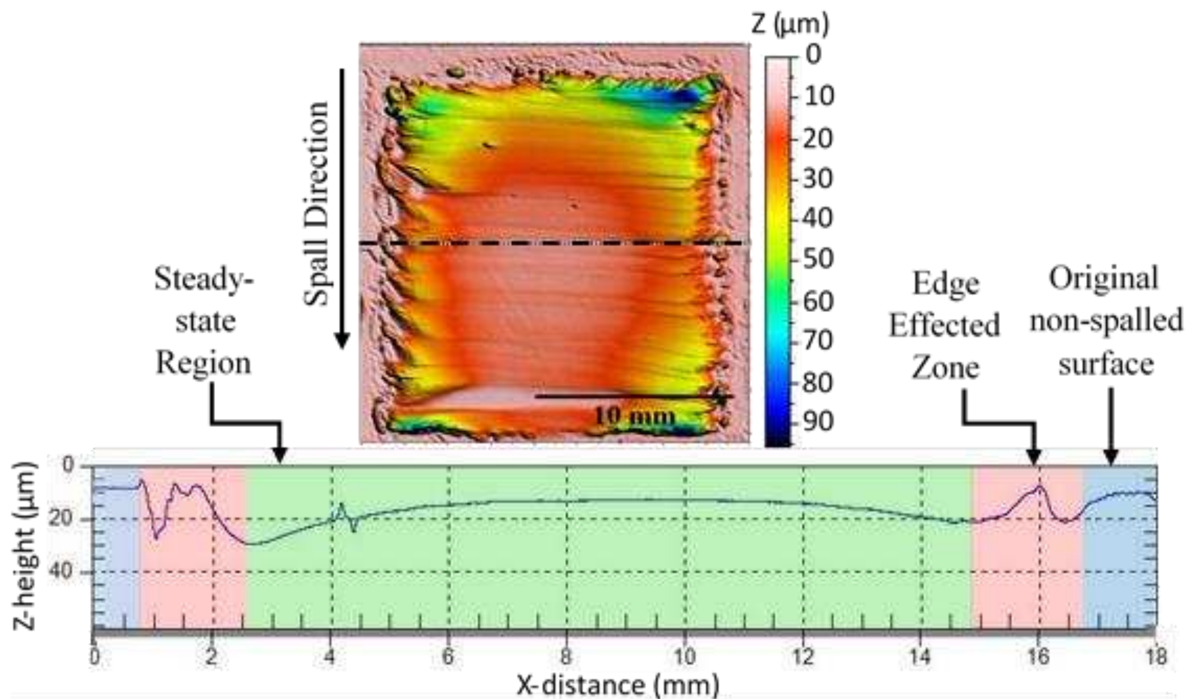


Figure 4.1: (top) Color height map of a spalled Ge substrate where higher Z values correspond to deeper areas relative to the original surface and (bottom) a profile scan positioned at the dashed line through the sample center with regions of interest highlighted

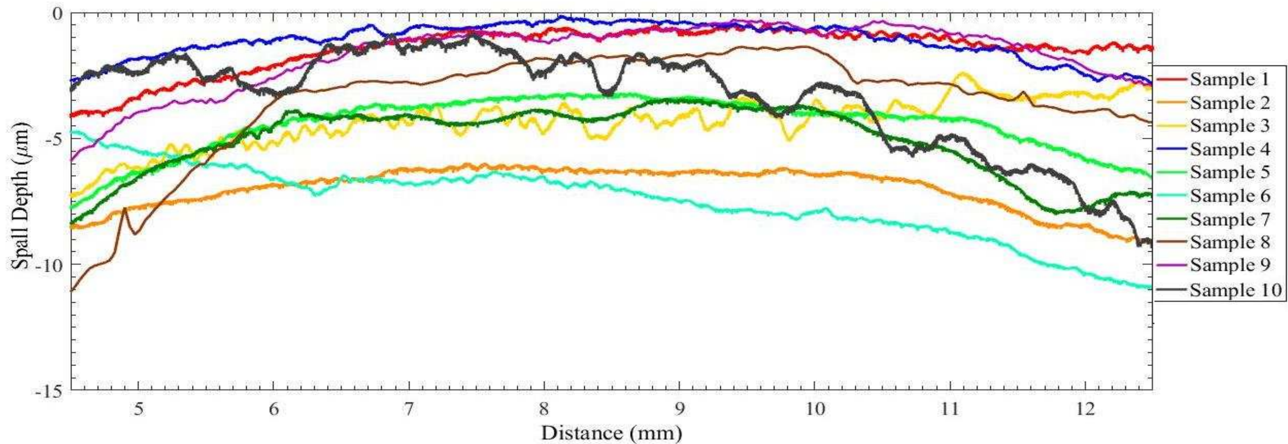

Figure 4.2: Line scans of the steady-state regions in 10 samples plated and spalled under the same conditions show significant spall depth changes between the sample center and the region edge

### 4.2 Steady-state Region: Surface Roughness

Substrate reuse requires a sufficiently smooth spalled surface for device growth, but improving spalled surface quality first necessitated isolating which features contributed the most to observed macroscale roughness. In Chapter 2, AFM scans over a 25-µm x 25-µm spalled area showed an RMS roughness of 2.3nm, which compared very well to the RMS roughness of 2.36nm measured on pristine Ge wafers. However, RMS roughness rapidly increased to 2.14µm over an 8-mm x 8-mm area scanned using laser profilometry. At the macroscale, parallel undulations oriented perpendicular to the spall direction can be observed throughout the entire steady-state area of Figure 4.1. Neither the perturbations nor the underlying semi-spherical nature of the spalled surface was detected during AFM scanning. However, both contribute significant surface roughness at the macroscale. To compare the roughness induced by each factor, a representative set of spalled samples were scanned and inherent curvature of the surface removed using TrueMap's least-squares polynomial form removal tool. Figure 4.3 (see page 41) shows the center 8-mm x 8-mm area of a representative spalled substrate before and after form removal was applied. Parallel undulations can be observed in Figure 4.3(a), but their contributions to spall depth

variation are masked by the surface's semi-spherical nature which resulted in a 14µm spall depth difference between the sample center and the edges. Once the surface curvature was removed, as shown in Figure 4.3(b), the undulations and sporadic pits were observed to vary <1µm in height (see Figure 4.3(c)). RMS roughness calculations confirmed that across ten spalled samples removed of curvature, the perturbations represented on average 0.61±0.20µm over an 8-mm x 8-mm area. Comparatively, the features were substantially smaller than nominal 5µm facets achieved by spalling along complementary {110} cleavage planes in (100) GaAs. [17] The RMS roughness values calculated before and after form removal on five representative samples in the set are summarized in Table 4.1: Representative roughness measurements over 8-mm x 8-mm spalled areas before and after form removal The roughness measured prior to flattening typically exceeded 2µm, which is substantially larger the than sub-micron undulations. This suggests that if the semi-spherical nature of the surface can be lessened or removed, it is likely sub-micron height variation will dominate.

Table 4.1: Representative roughness measurements over 8-mm x 8-mm spalled areas before and after form removal

| | **Surface Roughness, $R_q$ (µm)** | |
|---|---|---|
| **Sample ID** | **Original Surface** | **Leveled Surface** |
| **FF031** | 3.9 | 0.29 |
| **FF032** | 9.33 | 0.43 |
| **FF033** | 2.58 | 0.71 |
| **FF034** | 4.1 | 0.29 |
| **FF035** | 2.14 | 0.54 |

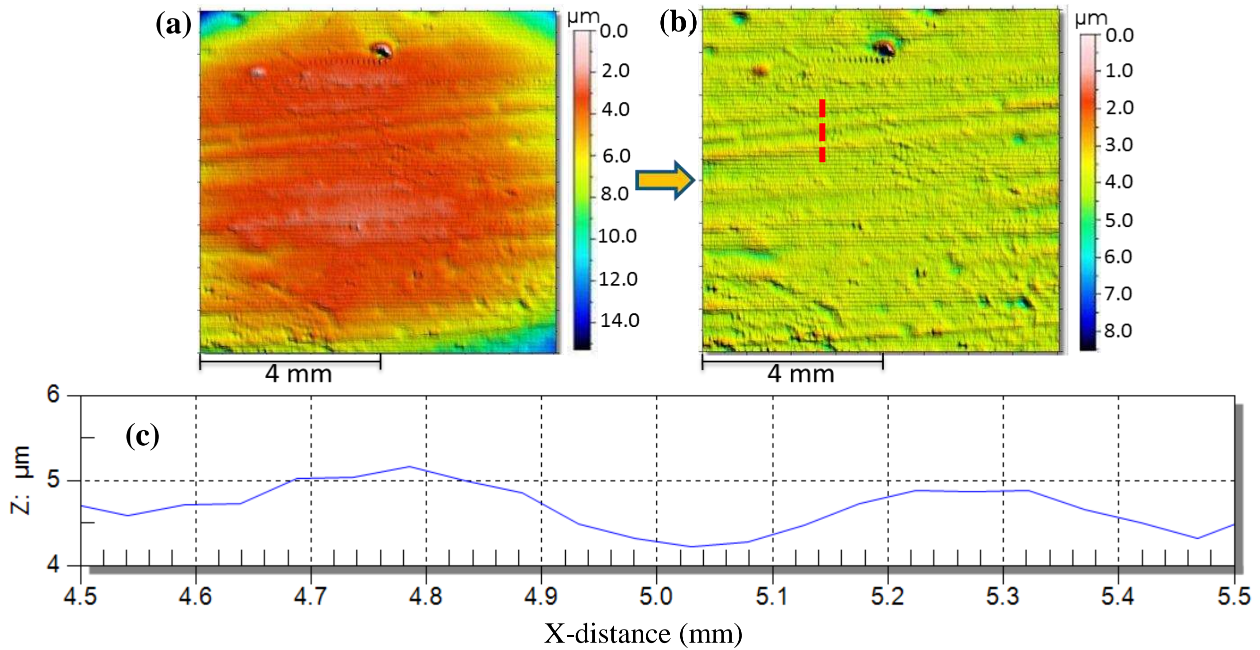


Figure 4.3: a) A representative laser scan of a spalled surface at the sample center, b) the same surface after form removal, and c) the surface profile across two undulations which intersect the red-dashed line in (b)

## 4.3 Arrest Lines

Nearly parallel undulations observed throughout the spalled area were characterized as crack arrest lines. Fractography analysis of the spalled surfaces, shown in Figure 4.4(a) (see page 42), revealed the undulations were defined by two low-angle planes and the fracture surfaces on each side of the feature followed a different cleavage plane. Both characteristics of the discontinuity and surrounding fractured surfaces are hallmarks of established crack arrest behavior. [48] Arrest lines are produced when the driving force for crack growth relaxes below a critical value and a moving crack slows to a halt at a slightly different angle than the preceding cleavage plane. [40], [49] When the load increases again the crack re-initiates and resumes propagation at a slightly different direction. The process leaves behind well-defined striations which follow the shape of the crack front. Figure 4.4(b) shows a representative cross section of the arrest line features observed on the spalled (100)-Ge surface.

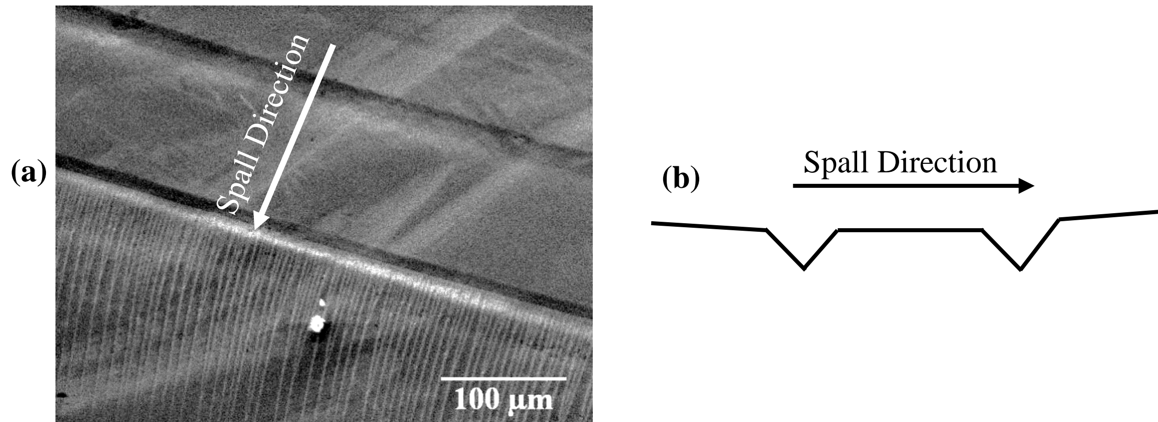


Figure 4.4: (a) Top-down SEM view of two arrest lines on spalled Ge and (b) a representative cross section view of the same surface (not to scale). Low angle planes define the arrest line and fractured surfaces on each side of an arrest front lie on a different plane.

Arrest lines also lack crystallographic dependency and are generally oriented parallel with the crack front (or perpendicular with the propagation direction). [48] To confirm the undulations were arrest lines, an experiment was conducted to determine the influence of spall direction on the orientation of the features. Therefore, ten samples electroplated under the same conditions were rotated 45° such that fracture was intentionally initiated at a corner rather than along an edge. Figure 4.5 (see page 43) shows two substrates spalled from different directions with black arrows representing the orientation of the undulations. Since the features clearly rotated to maintain perpendicularity relative to roller direction, the spalling process utilized in this study must have been the cause of the arrest line formation as the crystallography differs for the two spall directions. Comparatively, Bedell et al. similarly reported start-stop features (or arrest lines) on spalled Ge surfaces using roller initiated spalling similar to one utilized in this study. [28] They attributed the fracture depth variations to non-constant spalling velocity and speculated automating the spalling process could minimize the defects. In this study, the roller initiated a crack and guided spalling at an average 1.05 m/s, but Greenwood et al. measured the minimum fracture velocity along a non-crystallographic direction in Ge on the order of 300m/s. [50] Based on that knowledge it is possible

the arrest lines were generated by the disparity between roller velocity and the velocity of the propagating crack front. A plausible explanation for the generation of arrest lines include the following steps: (1) During spalling, the roller-exerted force produced enough change in stress intensity at the crack tip to drive propagation a few millimeters in front of the roller position. (2) The imparted energy was consumed by generation of new fracture surfaces, and the crack stopped advancing. (3) Less than a millisecond passed before the roller caught up and exerted force again, which reinitiated fracture and left behind a crack arrest line. (4) Finally, the stop-and-go pattern was repeated through the entire spalling process, thereby producing nearly parallel arrest lines throughout the entirety of the spalled region. Guided by this basic theory, the future works section of this thesis recommends several modifications to the spalling process to resolve formation of these features which will be addressed by further research under the project funding.

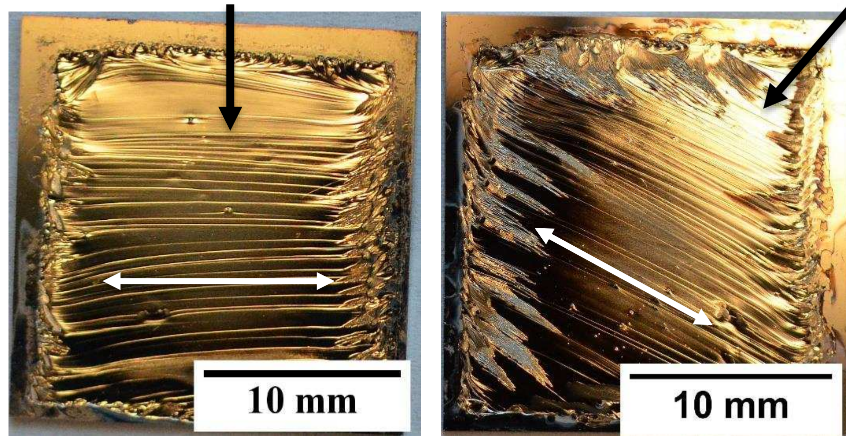


Figure 4.5: Ge substrates spalled from two different directions. Black arrows represent crack propagation direction and white arrows represent orientation of the generated undulations

### 4.4 Edge-affected Zones

Along the spalled area perimeter and particularly near the corners, spall depth extends more than 50μm into the wafer for samples with spall depths measuring <5μm at the sample's center. Furthermore, optical microscopy showed out-of-plane branching structures which extended 1-2

mm into the spalled area. These features drastically increased surface roughness and reduced potential device growth area up to 20%. Fractography analysis of features observed on the fractured surface provided useful insight into the loading modes present during spalling. In sub-section 4.4.1, observations of river line patterns at arrest lines and in featureless regions of fractured surfaces are discussed. Sub-section 4.4.2 addresses the fracture behavior of twist hackle generated near plated edges and corners. Finally, mixed-mode loading conditions induced during spalling are explained in relation to the generation of these features.

### 4.4.1 River Line Patterns

Mode I/III loading within edge-affected zones was confirmed by the presence of river line patterns, which are unique to this loading condition. Figure 3.3 represents the top-view of a spalled Ge substrate imaged by white-light digital microscopy. The surface features within the top-left corner of the same sample were analyzed under different magnifications. The macroscopic appearance of the analyzed region is shown in Figure 4.7(a) (see page 46). This figure exhibits two distinct features: (1) arrest lines oriented perpendicular to spalling direction and (2) branching features oriented parallel with spall direction. Magnification at one of the arrest lines resolved hundreds of closely spaced steps initiated along the arrest line, as depicted in Figure 4.7(b). The steps merged progressively into larger steps in the general direction of crack propagation, which are characteristic features of river line patterns. [51] While the features in this study primarily nucleated at arrest lines, many river line patterns were found to initiate within featureless regions and propagate through the undulations, as shown in Figure 4.7(c). Therefore, solving arrest line development will not completely prevent these features from arising. At higher magnifications, the branching effect and a minimum spacing between steps of about 1.5μm was clearly observed, shown in Figure 4.7(d). The branching behavior and spacing between each crack correlated well

with micrographs of river patterns generated within cured epoxy resin, see Figure 4.6. [51] In the figure, the mode III component was kept low and then increased when the fracture front reached boundary A-B after which the size of the river patterns dramatically increased. For this study, the similarities between the high mode III features and river patterns observed at the plated edges suggests the crack tip experienced similarly high mode III loading in that region. In mode III loading, shear stress acts parallel to both the crack tip and the plane of the crack. When both mode I and III are present during crack growth, river line patterns are the most characteristic features to appear on fracture surfaces in both amorphous and crystalline brittle materials. [51] The mixed-mode loading causes the axis of principal stress to tilt to tilt away from the original orientation. The crack is unable to rotate all at once in response to the new stress direction, so it breaks into small unconnected segments advancing at different rates. [52] Some studies have suggested the patterns are produced when cracks intersect dislocations with screw components. [51], [53] However, previous metallographic studies revealed screw dislocations were not present at initiation points of river patterns generated on germanium surfaces. [54] Furthermore, spalling has

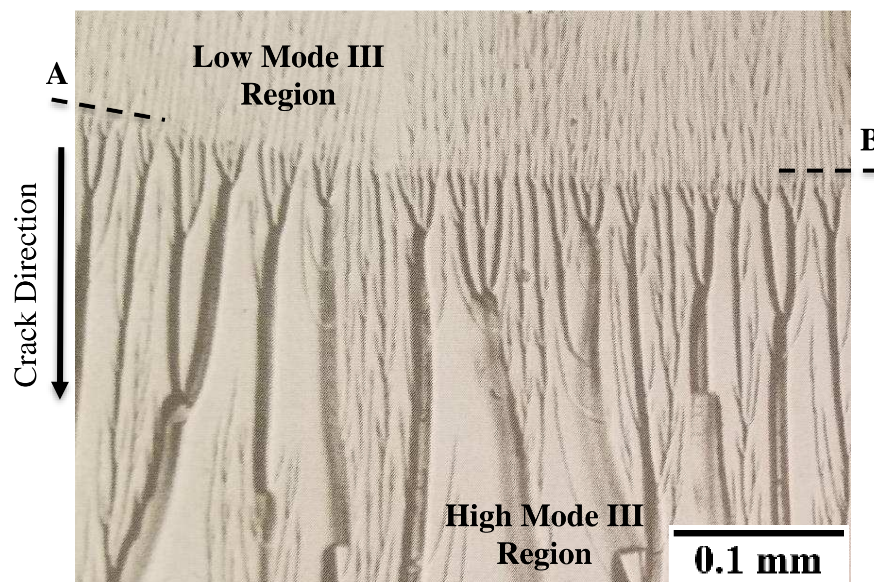


Figure 4.6: River patterns on fracture surface of epoxy resin tested in mixed-mode I/III loading as adapted from Ref. [51]

been shown not to introduce dislocations in GaAs systems. [17] It is similarly expected spalling has not induced dislocations in the substrate and these features were produced by mixed-mode loading rather than crack interactions with dislocations.

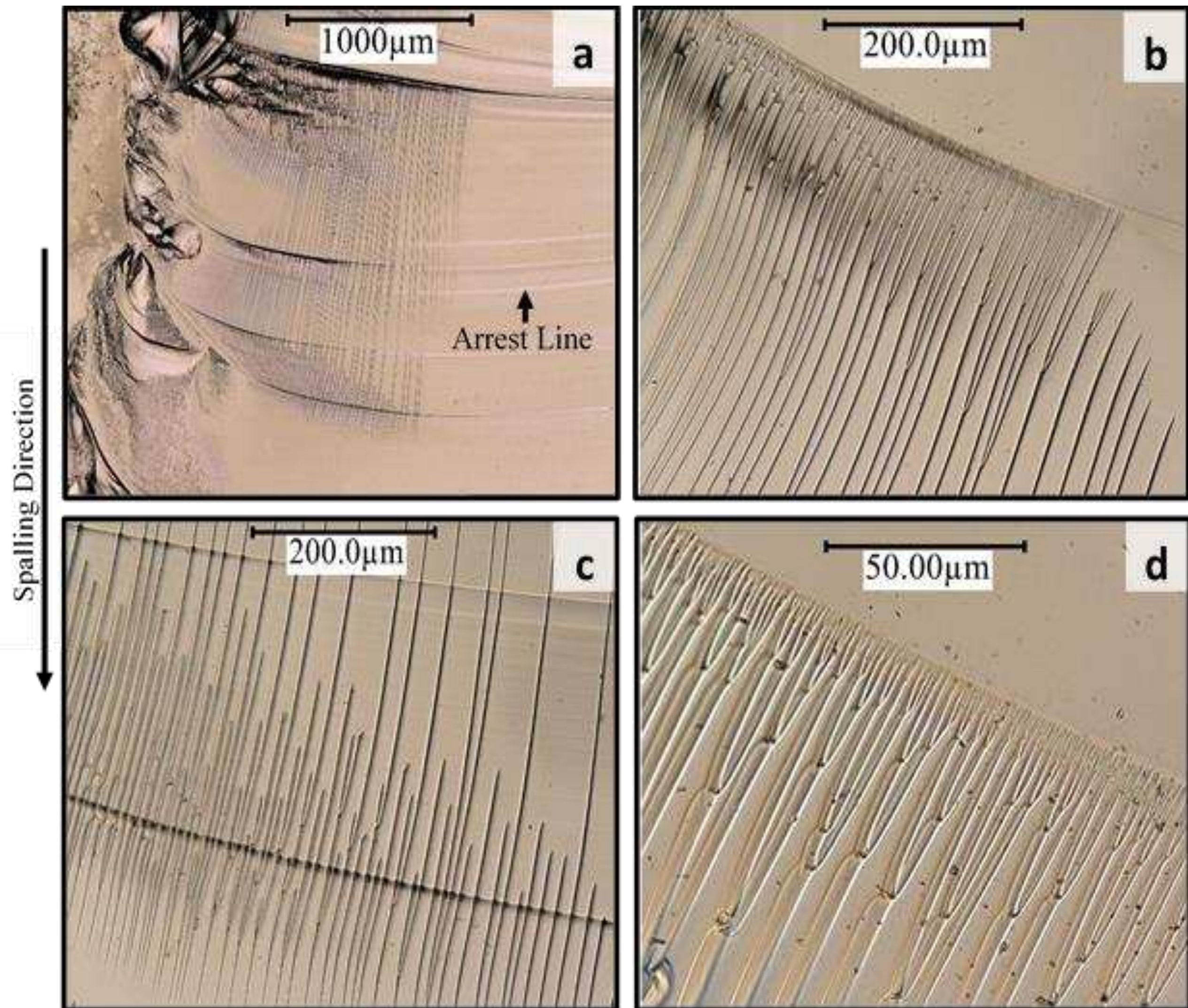


Figure 4.7: Digital micrographs of fractured surfaces showing (a) the top-left corner of a spalled region, (b) merging of river patterns with distance away from an arrest line, (c) high magnification of river patterns, and (d) river line patterns extending through arrest lines

### 4.4.2 Twist Hackle

Another suggestive feature of mixed-mode loading is the presence of twist hackle, also known as lances or shear hackle, in the immediate vicinity of plated edges and corners. As shown in Figure 4.9 (see page 48), progressive ridges or twist hackle were oriented perpendicular to the main spalling direction near the edge of a spalled area. The color spread observed in this figure is attributed to the lighting conditions interacting with a thin film of residual etchant rather than any microstructural concerns. Twist hackle is generated by the primary crack as it travels around corners or geometric irregularities and meets abrupt changes in the stress field due to mixed-mode loading. [40] The feature is a form of hackle defined by portions of the crack surface separated into steps. Similar to river line patterns, each step is rotated in response to the change in the direction of maximum principle stress induced by mode III loading. [55] Contrary to the behavior of river line patterns and velocity hackle, twist hackle follows the direction of local crack propagation which may not be aligned with the main crack direction. [56] An edge view of representative twist hackle is depicted in Figure 4.8 (see page 48) in which the vertical steps are induced by the opening mode. [57] In the figure, mode III loading is aligned with the local direction of crack direction thereby driving the crack extension toward the sample edge where realignment with the principle stress state requires minimal energy. Similarly, the features observed in Figure 4.9 follow a local crack direction toward the sample edge rather than the main spalling direction. This behavior suggests mode III components at the plated edges dominated over the mode I causing crack propagation oriented toward the sample edges.

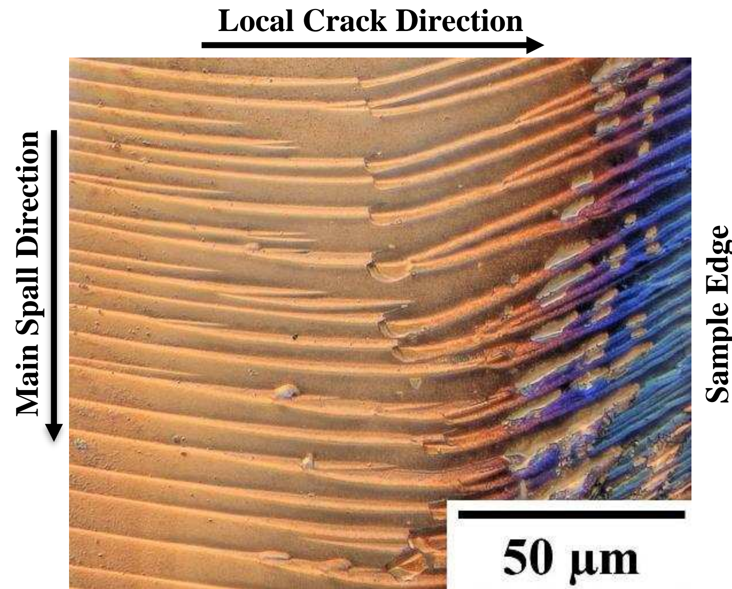


Figure 4.9: Twist hackle formed at a plated edge oriented perpendicular to main spalling direction (or mode I component) but parallel with the local mode III component

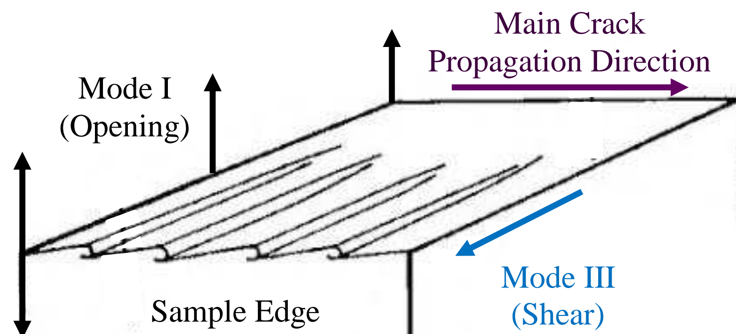


Figure 4.8: General twist hackle generation from mixed-mode loading as adapted from Ref. [57]. Local direction of fracture is aligned with the mode III component.

### 4.4.3 Mixed Mode Loading Conditions

The river line patterns and twist hackle were produced when anisotropic stress states generated during high-speed electroplating caused mixed-mode loading within the deposited film. Due to the high plating rate and bath chemistry, the electroplated Ge substrate was under biaxial tension in the center of the sample, which implies stress in any two perpendicular directions in the plane of the film were equal and pulling inward. Near the edges of the plated area, the stress field

was still biaxial, but the stress components were not equal due to the presence of the plating zone edge. In Figure 4.10(a), a top-view schematic of a plated Ge substrate shows the assumed locations of these biaxially equal and anisotropic stress elements. As shown in the cross-section view, Figure 4.10(b), non-balanced stress tensors at the edges generated shear components orthogonal to the crack propagation direction during spalling. During a spall, the spatially varying stress field at the outer edges induced (shear) mode III loading. The (opening) mode I driven by the roller and mode III component from the residual film stress interacted to form an effective double moment in front of the crack tip near plated edges. Figure 4.11 (see page 50) shows the effective moments induced by the mixed-mode loading conditions within this region during controlled spalling. The mode III stress had the effect of rotating the crack front about an axis parallel with the fracture direction. As such, cracks propagating in this region rotated out of the plane which resulted in river line patterns and twist hackle. Bedell et al. similarly noted roughening of a spalled surface due to competition between spalling and a mode III stress in a recent patent. [58] Following from the strong correlation between their work and this study, it is believed minimization of the mode III component through engineering solutions could drastically improve the spalled surface quality and increase the reusable area.

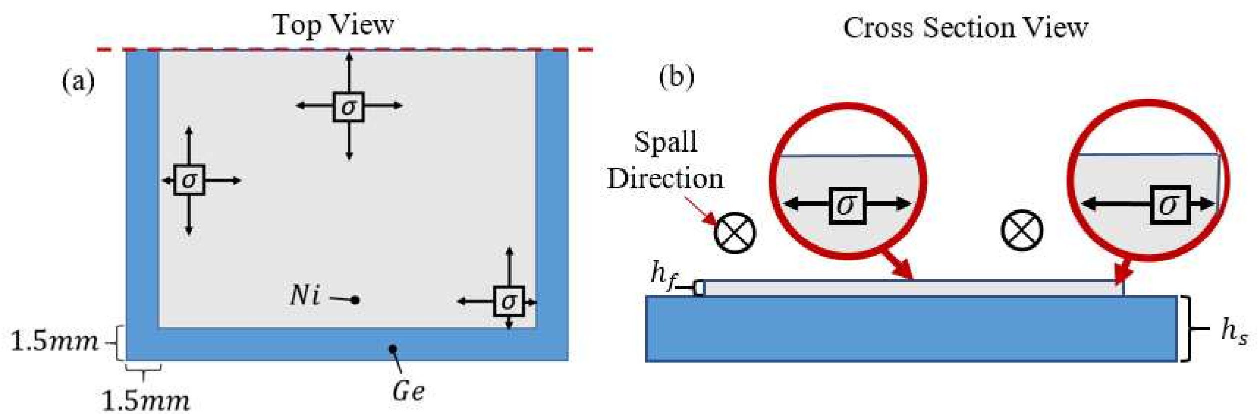


Figure 4.10: The relative magnitude of tensile stress components at different locations within the deposited Ni layer from a planar view (a) and a cross section view (b)

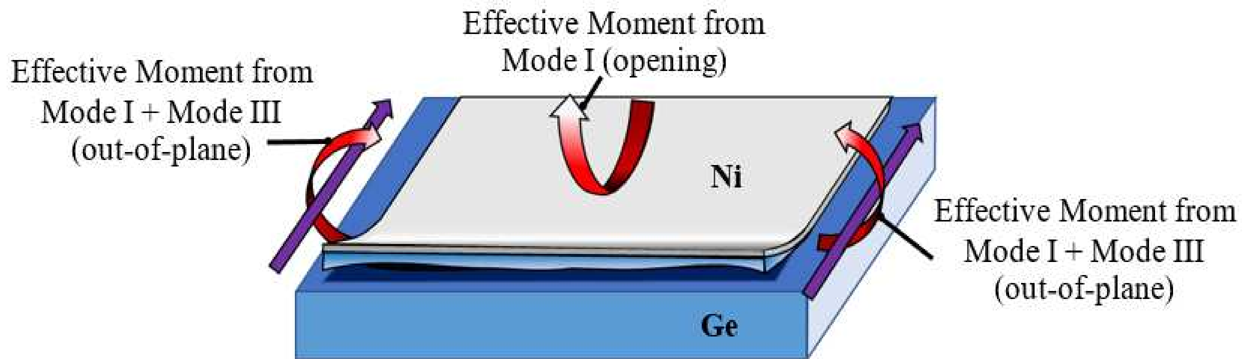


Figure 4.11: Schematic of moments induced on plated substrates at spalling fracture initiation. Purple arrows represent crack propagation direction and red arrows represent the moments induced by the roller and anisotropic stress states within the Ni film.

### 4.5 Chapter Summary

For this study, the fracture behavior of Ge substrates is defined by a steady-state region near the sample center and spall depth excursions known as edge-effects along the inside perimeter of the spalled area. Within the steady-state region, the fracture surface followed a distinct semi-spherical nature leading to increased material consumption away from the sample center. This macro-scale curvature was found to contribute substantially more to RMS roughness than sub-micron arrest lines observed throughout the spalled area. If the semi-spherical behavior was resolved, it is possible sub-micron height variation will dominate over an 8-mm x 8-mm area of the spalled area. Within the edge-affected zones, river patterns extended into the spalled area over a few millimeters, which significantly reduced useable device area and the prospect of wafer reuse for the technology. River line patterns were typically initiated at arrest lines and oriented parallel with the spalling direction. Twist hackle, however, was oriented perpendicular to the spall direction and constrained to edges and corners of the spalled area. Both features were found to initiate within featureless regions which provides strong evidence their generation is caused by mode I and mode III loading during spalling.

# CHAPTER 5 SUMMARY AND CONCLUSIONS

The motivation for this work was to utilize spalling fracture to exfoliate Ge films of various thickness and demonstrate a critical step in the path towards wafer reuse of single-crystal substrates. Compared to conventional lift-off methods, spalling via electrodeposition can be easily incorporated with device fabrication methods with minimal capital input. Furthermore, several plating conditions can be tailored to induced exfoliation over a wide range of depths applicable to flexible devices. One demonstration of substrate reuse enabled by controlled fracture was presented by collaborating with NREL to process functioning III-V devices on spalled-Ge. Fracture along a steady-state spall depth produced the highest material quality but significant improvement is still desired. This thesis concludes with a summary of the study results as well as remarks regarding the technological implications for a variety of applications.

## 5.1 Effects of Bath Chemistry and Plating Parameters on Spall Depth

In Chapter 2, the effects of plating parameters and electrolytic bath chemistry on controlled spalling conditions were investigated. For the first time, combinations of electroplating current density and plating time that allows controlled exfoliation of Ge films was reported. Controlled spalling conditions for three bath chemistries (Watts Nickel, a 5mM phosphorous acid solution, and a 10mM phosphorous acid solution) were enveloped by spontaneous spalling and sub-critical regions. Both critical plating density and average Ni stressor layer thickness decreased with increased phosphorous content. Suo & Hutchinson's linear elastic fracture mechanics predicted an increase in spall depth as a function of stressor layer thickness, which was supported by experimental thickness measurements of Ge films prepared by controlled spalling; this agreement provided further evidence that the fracture mechanics of spontaneous spalling have some

application to controlled spalling conditions. Among all three bath chemistries, a spall depth range of approximately 0.3-76µm into single-crystal (100)-oriented Ge was achieved. This chapter presents the first sub-7µm spalled-Ge films, which provides a pathway to drastically minimize material waste during lift-off of 3-5µm thick devices. Tensile residual stress within the deposited Ni layer was found to substantially rise with increased phosphorous concentration even though current density requirements for controlled spalling decreased. Thus, bath chemistry is believed to be the primary driver of increased stress levels from 90-2000 MPa, with current density providing an additional fine control parameter. These results strongly suggest that controlled spalling is a fast method which can be tuned via electroplating conditions and bath chemistry to exfoliate films of material or devices for a variety of applications, including high-performance flexible electronics.

## 5.2 Substrate Reuse for Photovoltaics Applications

The technological implications of controlled exfoliation are evident an initial demonstration of combining substrate reuse together with the ability to grow III-V solar cells at a very high growth rate. Prototype single-junction GaInAsP solar cells epitaxially grown on spalled (100)-Ge substrates and co-loaded pristine substrates measured equivalent efficiency of ~8% under one-sun. These are the first reported devices grown on spalled Ge substrates without additional surface preparation. Furthermore, this is the first demonstration of functional devices grown on spalled-Ge using high-throughput hydride vapor phase epitaxy. Sufficient surface quality of spalled-Ge for epitaxial growth was also evident by single-crystal growth of GaAs layers despite the lack of any additional surface preparation. The results present a promising path toward low-cost III-V photovoltaics; however, significant challenges need to be addressed to progress viability of substrate reuse. Future efforts will focus on ex-situ surface preparation to improve the

morphology of the spalled-Ge surface. While the quality of initial GaAs buffers on bulk and spalled-Ge is promising, the cell growth conditions are far from optimal. Lowering the base doping to improve the carrier collection and incorporating a passivating InGaP window layer are expected to improve the overall performance.

### 5.3 Fractography of Spalled (100)-Oriented Ge

For this project, understanding the origins of undesirable topographical features on spalled surfaces was critical for future improvements to spalling and subsequent epitaxial growth. Fractography analysis of the spalled area revealed two regions each characterized by distinct surface features. The first region occurred near the sample center where steady-state fracture dominated during exfoliation. Within the steady-state region, the fracture surface exhibited a semi-spherical shape such that material consumption increased radially away from the sample center. The results suggest investigating the underlying causes of non-planar fracture could have the greatest improvement on macro-scale roughness and could reduce material loss for substrate reuse applications. Arrest lines oriented perpendicular to the crack direction were present throughout this region and suggested inconsistent fracture propagation. It is plausible that instituting a non-roller method of exerting external force which allows crack propagation at constant nominal velocity will resolve the generation of arrest lines. The second region, known here as edge-affected zones, was defined by significant spall depth variation and roughness along the inside perimeter of the spalled area. Within these zone, river line patterns were oriented parallel with the spalling direction whereas twist hackle was observed perpendicular to the spall direction. Since both features initiate within featureless regions, their generation strongly suggests the presence of mode III loading during spalling. Although studies have shown spalling does not generate dislocations in (100)-GaAs, defects can form near nucleation regions of the twist hackle and river line patterns,

which should be further investigated as their presence could hinder high-quality epitaxy. The formation of edge-affected zones can significantly reduce useable device area and the prospect of wafer reuse for the technology. Commercial viability of substrate reuse enabled by controlled spalling depends on engineering solutions to minimize mixed-mode loading during exfoliation.

# BIBLIOGRAPHY

[1] C. Cheng, K. Shiu, N. Li, S. Han, L. Shi, and D. K. Sadana, "epitaixal lift-off process for gallium arsenide substrate reuse and flexible electronics," *Nat. Commun.*, vol. 4, p. 1577, 2013.

[2] J. Adams *et al.*, "Demonstration of multiple substrate reuses for inverted metamorphic solar cells," *IEEE J. Photovoltaics*, vol. 3, no. 2, pp. 899–903, 2013.

[3] G. J. Bauhuis, P. Mulder, and J. J. Schermer, "Thin-Film III–V Solar Cells Using Epitaxial Lift-Off," in *High Efficiency Solar Cells: Physics, Materials, and Devices*, vol. 190, X. Wang and Z. Wang, Eds. Springer, 2014, p. 664.

[4] J. Wang *et al.*, "Demonstration of thin-film GaN Schottky diodes fabricated with epitaxial lift-off," *Device Res. Conf. - Conf. Dig. DRC*, vol. 2016–Augus, no. 6, pp. 181–182, 2016.

[5] J. Kepa, R. Martini, and A. Stesmans, "Structural damage in thin SLIM-Cut c-Si foils fabricated for solar cell purposes: atomic assessment by electron spin resonance," *Semicond. Sci. Technol.*, vol. 30, no. 11, p. 115015, 2015.

[6] A. Masolin *et al.*, "Evidence and Characterization of Crystallographic Defect and Material Quality after SLIM-Cut Process," *MRS Proc.*, vol. 1323, 2011.

[7] V. Steckenreiter, J. Hensen, A. Knorr, S. Kajari-schr, and R. Brendel, "Reuse of Substrate Wafers for the Porous Silicon Layer Transfer," *IEEE J. Photovoltaics*, vol. 6, no. 3, pp. 783–790, 2016.

[8] J. Pan, J. Cooper, M. Melloch, S. material, and M. Bruel, "Silicon on insulator material technology," *IEEE Trans. J. Appl. Phys. J.w. Priv. Commun. Int. Symp. Comp. Semi. J. Electron. Mater*, vol. 75, no. 31, pp. 41–3205, 1994.

[9] R. Meyer, O. Kononchuck, H. Moriceau, M. Lemiti, and M. Bruel, "Study of high-temperature Smart Cut™: Application to silicon-on-sapphire films and to thin foils of single crystal silicon," *Solid. State. Electron.*, vol. 115, pp. 225–231, 2016.

[10] B. Geetha Priyadarshini, S. Aich, and M. Chakraborty, "Structural and morphological investigations on DC-magnetron-sputtered nickel films deposited on Si (100)," *J. Mater. Sci.*, vol. 46, no. 9, pp. 2860–2873, 2011.

[11] J. Dennis, "Nickel and Chromum Plating," in *Nickel and Chromum Plating*, 3rd ed., T. Such, Ed. Cambridge: Woodhead Publishing Limited, 1993, p. 438.

[12] G. a. Di Bari, "Electrodeposition of Nickel," *Mod. Electroplat. Fifth Ed.*, pp. 79–114, 2011.

[13] Z. Suo and J. W. Hutchinson, "Steady-state cracking in brittle substrates beneath adherent films," *Int. J. Solids Struct.*, vol. 25, no. 11, pp. 1337–1353, 1989.

[14] J. W. Hutchinson and Z. Suo, "Mixed Mode Cracking in Layered Materials," *Adv. Appl. Mech.*, vol. 29, pp. 63–191, 1991.

[15] C. A. Sweet, “Spalling Fracture Behavior In (100) Gallium Arsenide,” Colorado School of Mines, 2016.

[16] C. A. Sweet *et al.*, “Controlled exfoliation of (100) GaAs-based devices by spalling fracture,” *Appl. Phys. Lett.*, vol. 108, no. 1, 2016.

[17] C. A. Sweet, J. E. McNeely, B. Gorman, D. L. Young, A. J. Ptak, and C. E. Packard, “Engineering controlled spalling in (100)-oriented GaAs for wafer reuse,” *2015 IEEE 42nd Photovolt. Spec. Conf. PVSC 2015*, no. 100, 2015.

[18] S. W. Bedell *et al.*, “Layer transfer by controlled spalling,” *PRiME_IEEE PhD Res. Microelectron. Electron.*, vol. 152002, p. 53901, 2013.

[19] B. P. Rand, J. Genoe, P. Heremans, and J. Poortmans, “Solar cell efficiency tables (version 49),” *Prog. Photovoltaics Res. Appl.*, vol. 25, no. 1, pp. 3–13, 2017.

[20] S. Ward *et al.*, “Techno-economic analysis of three different substrate removal,” *Prog. Photovolt Res. Appl.*, vol. 24, no. May 2016, pp. 1284–1292, 2016.

[21] R. a. Rao *et al.*, “A novel low cost 25μm thin exfoliated monocrystalline Si solar cell technology,” *2011 37th IEEE Photovolt. Spec. Conf.*, pp. 001504–001507, 2011.

[22] F. Dross *et al.*, “Stress-induced large-area lift-off of crystalline Si films,” *Appl. Phys. A Mater. Sci. Process.*, vol. 89, no. 1, pp. 149–152, 2007.

[23] S. W. Bedell, K. E. Fogel, B. Hekmatshoar-tabari, D. K. Sadana, G. G. Shahidi, and D. Shahrjerdi, “Multi-Junction Photovoltaic Device and Fabrication Method,” 2011.

[24] D. Shahrjerdi *et al.*, “High-efficiency thin-film InGaP/(In)GaAs/Ge multijunction solar cells enabled by controlled spalling technology,” *Conf. Rec. IEEE Photovolt. Spec. Conf.*, vol. 53901, pp. 974–977, 2012.

[25] E. U. Onyegam *et al.*, “Exfoliated sub-10μm thin germanium for cost-effective germanium based photovoltaic applications,” *Conf. Rec. IEEE Photovolt. Spec. Conf.*, pp. 000271–000273, 2011.

[26] J. Simon, D. Young, and A. Ptak, “Low-cost III-V solar cells grown by hydride vapor-phase epitaxy,” *2014 IEEE 40th Photovolt. Spec. Conf. PVSC 2014*, pp. 538–541, 2014.

[27] K. L. Schulte, W. L. Rance, R. C. Reedy, A. J. Ptak, D. L. Young, and T. F. Kuech, “Controlled formation of GaAs pn junctions during hydride vapor phase epitaxy of GaAs,” *J. Cryst. Growth*, vol. 352, no. 1, pp. 253–257, 2012.

[28] S. W. Bedell *et al.*, “Kerf-less removal of Si, Ge, and III-V layers by controlled spalling to enable low-cost PV technologies,” *IEEE J. Photovoltaics*, vol. 2, no. 2, pp. 141–147, 2012.

[29] S. W. Bedell, N. Sosa, K. Fogel, D. Sadana, and D. Shahrjerdi, “Multijunction photovoltaic cell fabrication,” US 2013/0000708, 2013.

[30] A. Alharbi, B. Nasri, T. Wu, and D. Shahrjerdi, “Advanced Integrated Sensor and Layer Transfer Technologies for Wearable Bioelectronics,” no. 718, pp. 157–160, 2016.

[31] D. Shahrjerdi *et al.*, “Advanced flexible CMOS integrated circuits on plastic enabled by controlled spalling technology,” *Tech. Dig. - Int. Electron Devices Meet. IEDM*, no. d, pp. 92–95, 2012.

[32] D. Shahrjerdi *et al.*, “Ultralight high-efficiency flexible InGaP/(In)GaAs tandem solar cells on plastic,” *Adv. Energy Mater.*, vol. 3, no. 5, pp. 566–571, 2013.

[33] A. G. Evans and M.-S. Hu, “The Cracking and Decohesion of Thin Brittle Films,” *J. Mater. Res.*, vol. 3, no. 5, pp. 1043–1049, 1988.

[34] A. Alharbi and D. Shahrjerdi, “Energy band engineering of flexible gallium arsenide through substrate cracking with pre-tensioned films,” *Phys. Status Solidi - Rapid Res. Lett.*, vol. 10, no. 8, pp. 627–633, 2016.

[35] Y. Kwon, C. Yang, S. H. Yoon, H. D. Um, J. H. Lee, and B. Yoo, “Spalling of a thin Si layer by electrodeposit-assisted stripping,” *Appl. Phys. Express*, vol. 6, no. 11, 2013.

[36] J. K. Luo, M. Pritschow, A. J. Flewitt, S. M. Spearing, N. a. Fleck, and W. I. Milne, “Effects of process conditions on properties of electroplated Ni thin films for microsystem applications,” *J. Electrochem. Soc.*, pp. 155–161, 2006.

[37] C. Oliver and M. Pharr, “An improved technique for determining hardness and elastic modulus using load and displacement sensing indentation experiments,” *Journal of Materials Research*, vol. 7, no. 11. pp. 1564–1583, 1992.

[38] G. C. A. M. Janssen, M. M. Abdalla, F. van Keulen, B. R. Pujada, and B. van Venrooy, “Celebrating the 100th anniversary of the Stoney equation for film stress: Developments from polycrystalline steel strips to single crystal silicon wafers,” *Thin Solid Films*, vol. 517, no. 6, pp. 1858–1867, 2009.

[39] S. W. Bedell, K. Fogel, P. Lauro, and D. Sadana, “Method for Improving Surface Quality of Spalled Substrates,” US 9308714 B2, 2016.

[40] D. W. Richerson, *Modern Ceramic Engineering properties, Processing, and Use in Design 3rd Edition*. Taylor & Francis, 2005.

[41] J. Salem, R. Rogers, and E. Baker, “Structural Design Parameters for Germanium,” 2016.

[42] P. Lemaitre, “Fracture toughness of germanium determined with the Vickers indentation technique,” *J. Mater. Sci. Lett.*, vol. 7, no. 8, pp. 895–896, 1988.

[43] A. J. Detor and C. A. Schuh, “Tailoring and patterning the grain size of nanocrystalline alloys,” *Acta Mater.*, vol. 55, no. 1, pp. 371–379, 2007.

[44] G. McMahon and U. Erb, “Structural transitions in electroplated Ni-P alloys,” *J. Mater. Sci. Lett.*, vol. 8, no. 7, pp. 865–868, 1989.

[45] B. P. Daly and F. J. Barry, “Electrochemical nickel–phosphorus alloy formation,” *Int. Mater. Rev.*, vol. 48, no. 5, pp. 326–338, 2003.

[46] J. Simon *et al.*, “Upright and Inverted Single Junction GaAs Solar Cells Grown by Hydride Vapor Phase Epitaxy,” *Proc. 43rd IEEE Photovoltaics Spec. Conf.*, vol. 7, no. 1, pp. 4–7, 2016.

[47] N. Jain, J. Simon, K. L. Schulte, and A. Ptak, “18.7% GaInAsP Solar Cells Grown by HVPE for III-V/Si Photovoltaics,” Golden, 2017.

[48] D. Hull, “Fractography: Observing, Measuring and Interpreting Fracture Surface Topography,” in *Fractography: Observing, Measuring and Interpreting Fracture Surface Topography*, Cambridge: Cambridge University Press, 1999, pp. 273–278.

[49] S. Scherrer, J. Quinn, G. Quinn, and A. Wiskott, “Fractographic ceramic failure analysis using the replica technique,” *Dent. Mater.*, vol. 144, no. 5, pp. 724–732, 2008.

[50] J. Greenwood, “The Measurement of Fracture Speeds in Silicon and Germanium,” *Int. J. Fract.*, vol. 8, no. 2, pp. 183–193, 1972.

[51] D. Hull, “Fractography: Observing, Measuring and Interpreting Fracture Surface Topography,” in *Fractography: Observing, Measuring and Interpreting Fracture Surface Topography*, Cambridge: Cambridge University Press, 1999, pp. 91–119.

[52] D. Hull, “The effect of mixed mode I/III on crack evolution in brittle solids,” *Int. J. Fract.*, vol. 70, no. 1, pp. 59–79, 1994.

[53] J. J. Gilman, “Creation of cleavage steps by dislocation,” *Trans. Am. Inst. Min. Metall. Eng.*, vol. 212, no. 310–315, 1958.

[54] D. Haneman and E. N. Pugh, “Tear Marks on Cleaved Germanium Surfaces,” *J. Appl. Phys.*, vol. 34, no. 8, pp. 2269–2272, 1963.

[55] V. Frechette, “Markings on Crack Surfaces of Brittle Materials: A Suggested Unified Nomenclature,” *Am. Soc. Test. Mater.*, vol. STP, no. 827, pp. 104–109, 1984.

[56] G. Quinn, “Fractography of Ceramic and Glasses,” US GOVERNMENT PRINTING OFFICE, Washington D.C., 2007.

[57] G. D. Quinn, “A History of the Fractography of Glasses and Ceramics,” in *Fractography of Glasses and Ceramics VI*, John Wiley & Sons, Inc., 2012, pp. 31–32.

[58] S. Bedell *et al.*, “Method for Improving Quality of Spalled Material Layers,” 0034699 A1, 2014.

# APPENDIX A CAD FILES FOR ELECTROPLATING JIG

This appendix provides an assembly view of the electroplating jig designed in SolidWorks 2016 and 3D printed using a LulzBot machine and PLA material, see Figure A.1. The relevant CAD drawings to reproduce this device is also presented. The part was printed 100% dense and removed of support material after printing. Compliant gasket material was inserted into the "Eplate Jig Bottom" square 2cm x 2cm inset. Copper-coated wires were threaded through the internal channels and exposed wires made contact with back of the "Ejig Cover". Copper tape was adhered to the backside of the cover, which created a front-contact bridge between the wafer surface and the wires when the system was in use.

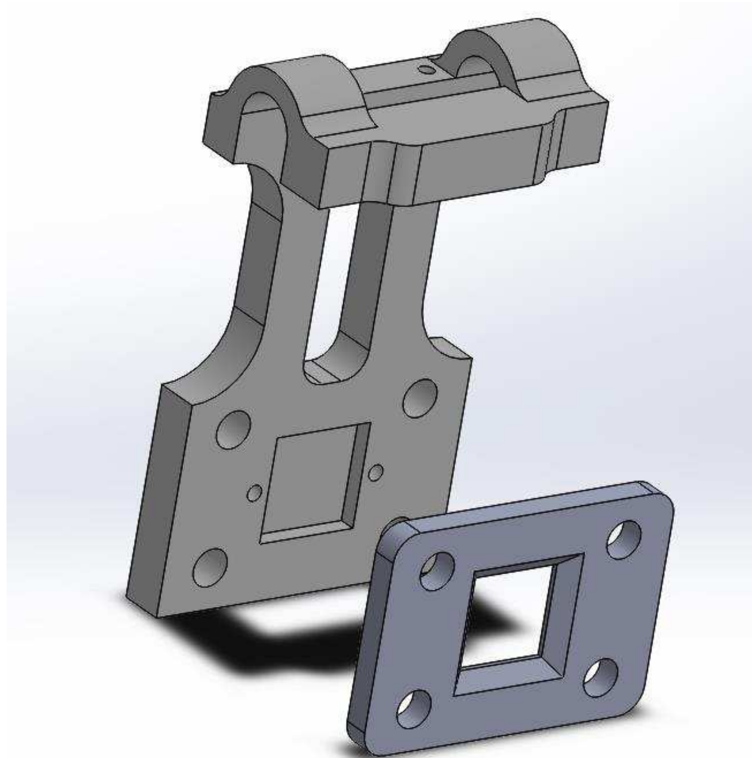

Figure A.1: Part assembly for electroplating jig used to hold 2cm x 2cm wafers

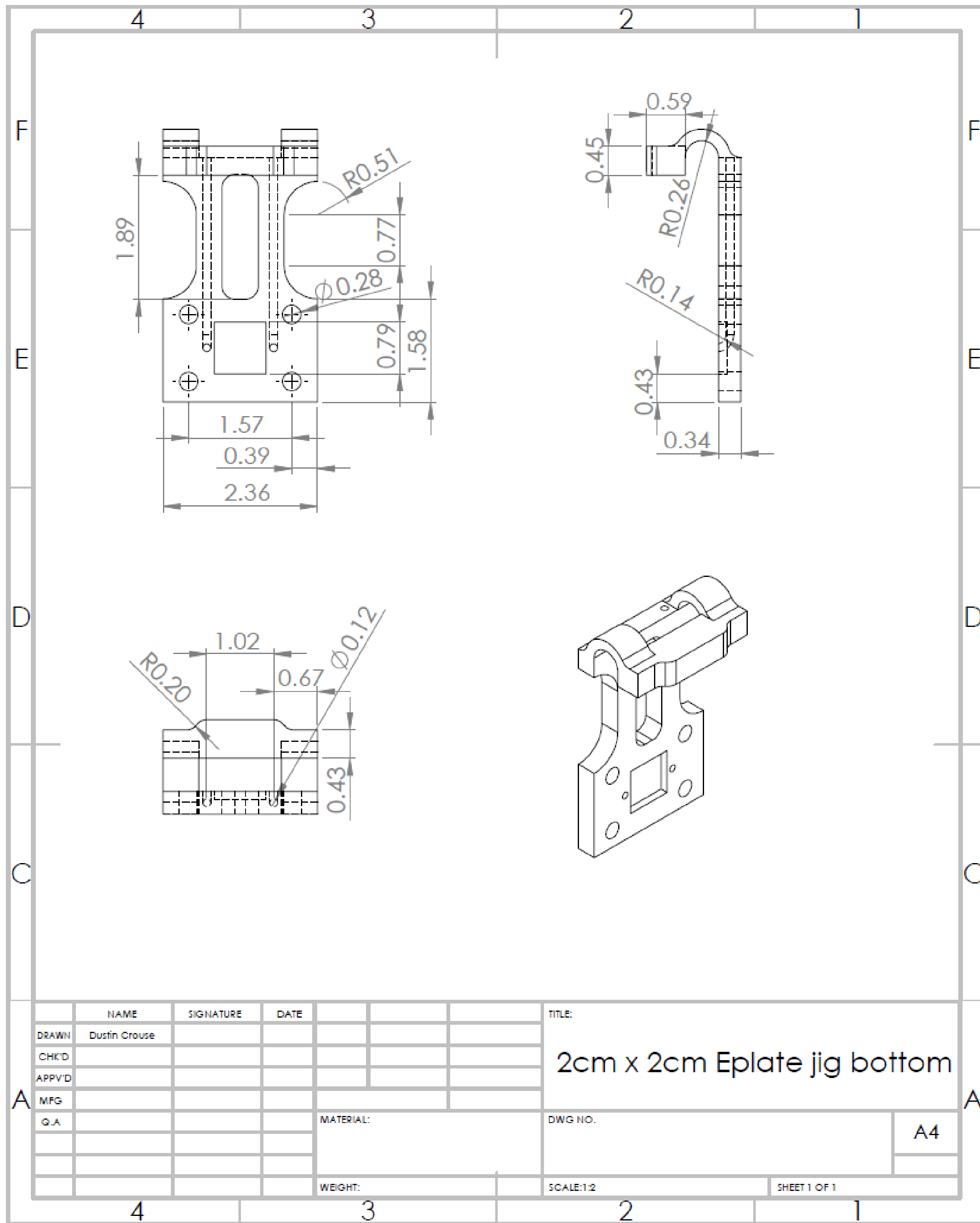


Figure A.2: SolidWorks drawing file demonstrating electroplating jig dimensions in different views

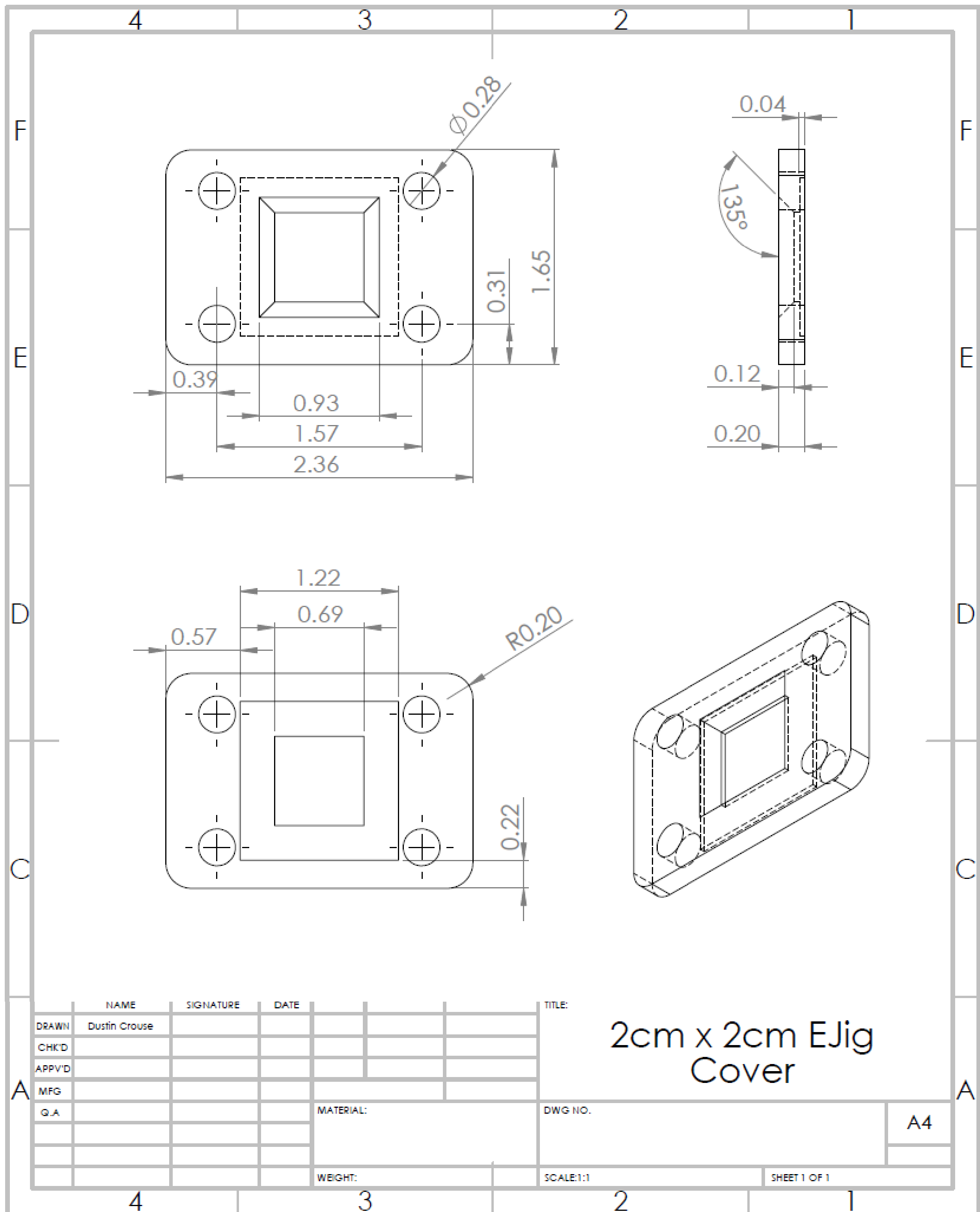


Figure A.3: SolidWorks drawing file demonstrating electroplating jig cover dimensions

# APPENDIX B MATHEMATICA MODELS OF LINEAR ELASTIC SPONTANEOUS FRACTURE IN GERMANIUM SUBSTRATES

The Mathematica code provided in this chapter were used to predict spall depth vs stressor layer thickness and residual stress vs stressor layer thickness following Suo and Hutchinson's models for spalling fracture of brittle substrates. Experimental data was also imported and overlaid on the predicted trends.

## Material Properties

```
v1=0.31;  (*Ni Poisson*)
v2=0.28; (*Ge Poisson*)

E1=201*10^9/(1-v1^2); (*E1=Stressor layer nanoindentation modulus: 220.84+/-20.08 GPa*)
E2=102.7*10^9/(1-v2^2); (*E2=Substrate Modulus*)

(* Lattice strain mismatch (alpha) takes into account the strain between the electroplated film and the
substrate due to differences in lattice size and arrangement *)
α=(E1-E2)/(E1+E2);

λo = 350*10^-6/h; (*Thickness of wafer in um divided by stressor layer film thickness 'h'*)

(* hh2 represents theoretical stressor layer film thickness.*)
hh2 = Range[0.01,65.01,0.2]*10^-6;
Length[hh2];
```

## Full Solution Equations

```
(* See the article: Z.Suo and J.W.Hutchinson,"Steady-state cracking in brittle substrates beneath adherent
films," Int.J.Solids Struct.,vol.25,no.11,pp.1337-1353 1989.*)
e=(1+α)/(1-α);
Δ=(λ^2+2e λ+e)/(2(λ+e));
Δo=(λo^2+2e λo+e)/(2(λo+e));
A=λ+e;
```

```
i=(e(3(Δ-λ)^2-3(Δ-λ)+1)+3Δ λ(Δ-λ)+λ^3)/3;
Ao=λo+e;
io=(e(3(Δo-λo)^2-3(Δo-λo)+1)+3Δo λo(Δo-λo)+λo^3)/3;
C1=A/Ao;
C2=A/io ((λo-Δo)-(λ-Δ));
C3=i/io;
p=σ h(1-C1-C2(1/2+λo-Δo));
m=σ h^2 ((1/2+λ-Δ)-C3(1/2+λo-Δo));
U=(1/A+1/(λo-λ)+(12(Δ+(λo-λ)/2)^2)/(λo-λ)^3)^-1 ;
V=(1/i+12/(λo-λ)^3)^-1;
w=52 Degree;
K1=p/√(2 h U) Cos[w]+m/√(2 h^3 V) Sin[w+y]; (*K1 stress intensity *)
K2=p/√(2 h U) Sin[w]-m/√(2 h^3 V) Cos[w+y]; (*K2 stress intensity *)
y=ArcSin[√(U V) 12 (Δ+(λo-λ)/2)/(λo-λ)^3];
```

## Theoretical Spall Depth Results

```
l=Table[FindRoot[ArcTan[K2/K1]==0,{λ,0.6}],{h,hh2}]; (*Find the root solutions where K2 = zero (i.e. steady state fracture)*)
Length[l];
rall=λ/.l;


(* Output a list of theoretical spall depth stemming from Suo and Hutchinson calculations partially taken from the paper, "Influence of substrate compliance on buckling delamination of thin films." *)
spallDepth=rall hh2;


(* Steady state spall depth using Ni modulus of 241 GPa *)
SpallDepth241GPa = {8.919721642276077`*^-8,1.7746370164079456`*^-6,3.3008069383958564`*^-6,4.69909391745993`*^-6,5.991894481603949`*^-6,7.195846127791214`*^-6,8.323704024556355`*^-6,………,0.00007163544037084694`};


(* Steady state spall depth using Ni modulus of 201 GPa *)
SpallDepth201GPa  = {7.098231642669272`*^-8,1.4271320379696964`*^-6,2.6775704707895095`*^-6,3.839980621609511`*^-6,………,0.00006910313791221765`};


(* Organize results into (x1,y1), (x2,y2), etc. format *)
SpallDepth241GPa=Transpose[{hh2 10^6,SpallDepth241GPa 10^6}];
```

```
SpallDepth201GPa = Transpose[{hh2 10^6,SpallDepth201GPa 10^6}];

yAxis = Style["Spall Depth (μm)",16,FontFamily->"Arial"];

xAxis = Style["Nickel thickness (μm)",16,FontFamily->"Arial"];

xpos = 0.3; (* x-position of legend *)

ypos = 0.9; (* y-position of legend *)

swatchLegend = Placed[SwatchLegend[{"E_Ni = 221±20 GPa"},LegendMarkerSize->14],{xpos,ypos}];

labelStyle =Directive[FontFamily->"Arial",Black,FontSize->16];


TheoreticalResults = ListPlot[{SpallDepth241GPa,SpallDepth201GPa},Joined->True,PlotLegends->
swatchLegend,Filling->{1->{2}},FillingStyle->Opacity[0.7],PlotStyle->{Purple,Purple},Frame->True,
FrameLabel->{xAxis,yAxis},PlotRange->{{0,65},{0,80}},LabelStyle->labelStyle]
```

## Import Experimental Data

```
(*First, look into excel file from which the data is imported.  Find the range or specific columns within
the file you want imported. Note, these columns must all be within the same excel sheet*)

importColumnRange = Join[{2 ,4,5,6},Range[10,13]];


(* Now the hard part. Find the file location C:\...... and name of the sheet in the excel file from which the
data will be imported.  The ExcelRows you specified above will be imported as well as all columns
within that sheet *)

rawData = Import["C:\Users\drc7a\Dropbox\Spalling Team Documents\Ge Spalling Project\Plating
Data\Plating Parameters.xlsx",{"Sheets","Thickness Measurements",All,importColumnRange}];

(* Unsuppress MatrixForm... to view the imported data in an easy-to-read structure*)


YN= Position[rawData[[All,1]],s_String/;StringMatchQ[s,"Y"] ] ;(* Find rows where answer to "Jig
spalled?" is a "Y" *)


(* Separate filtered rows into their respective bath chemistries *)

WattsNickelRows = Select[YN[[All,1]],#<= 62&];

TenMolarRows = Select[YN[[All,1]],63<= #<=137&];

FiveMolarRows = Select[YN[[All,1]],148<= #&];


(*StringTest= Position[rawData[[WattsNickelRows,2]],s_String/;StringMatchQ[s,""] ];*)

(* The measured stressor layer thickness for the samples that jig spalled. Column 2 = theoretical
thickness, Column 3 = measured thickness *)

WattsNiThickness= rawData[[WattsNickelRows,{3,4}]];

TenMolarNiThickness= rawData[[TenMolarRows,{2}]];
```

```
FiveMolarNiThickness= rawData[[FiveMolarRows,{3,4}]];

(* The measured spall depths for the samples that jig spalled. 5=Optically/SEM measured , 7=Mech profilometry *)
WattsSpallDepth= rawData[[WattsNickelRows, {5,6}]];
TenMolarSpallDepth = rawData[[TenMolarRows,{7,8}]];
FiveMolarSpallDepth= rawData[[FiveMolarRows,{5,6}]];

(* The imported experimental spall depth ranges *)
WattsSpallDepthRange = MinMax[WattsSpallDepth[[All,1]] ]
WattsNiThicknessRange = MinMax[WattsNiThickness[[All,1]] ]
TenMolarSpallDepthRange = MinMax[TenMolarSpallDepth[[All,1]] ]
TenMolarNiThicknessRange = MinMax[TenMolarNiThickness[[All,1]] ]
FiveMolarSpallDepthRange = MinMax[FiveMolarSpallDepth[[All,1]] ]
FiveMolarNiThicknessRange = MinMax[FiveMolarNiThickness[[All,1]] ]

(* Now organize the data into {x, y, ErrorX, ErrorY} format *)
OrganizedWatts=Transpose[Catenate[{{WattsNiThickness[[All,1]]},{WattsSpallDepth[[All,1]]},{WattsNiThickness[[All,2]]},{WattsSpallDepth[[All,2]]}}]];
OrganizedTenMolar=Transpose[Catenate[{{TenMolarNiThickness[[All,1]]},{TenMolarSpallDepth[[All,1]]},{TenMolarSpallDepth[[All,2]]}}]];
OrganizedFiveMolar=Transpose[Catenate[{{FiveMolarNiThickness[[All,1]]},{FiveMolarSpallDepth[[All,1]]},{FiveMolarNiThickness[[All,2]]},{FiveMolarSpallDepth[[All,2]]}}]];

(* Sometimes we don't have measurements for jig spalled samples so we are left with rows of missing data. The rows are in the form of empty strings {"","","",""}. The command below removes those empty rows for plotting *)
OrganizedWatts= DeleteCases[OrganizedWatts,{"","","",""}];
OrganizedFiveMolar= DeleteCases[OrganizedFiveMolar,{"","","",""}];
(* The 10mM bath does not have the same structure since it uses theoretical Ni thickness values. You must find rows with empty string "" in column 2*)
DeleteRows= Position[OrganizedTenMolar[[All,2]],s_String/;StringMatchQ[s,""] ] ;
OrganizedTenMolar= Delete[OrganizedTenMolar,DeleteRows]; (*Delete any row that was found to have an empty string *)

Needs["ErrorBarPlots`"] ;
OrganizedWatts = {{#1,#2},ErrorBarPlots`ErrorBar@@{#3,#4}}&@@@OrganizedWatts;
```

```
OrganizedFiveMolar = {#1,#2},ErrorBarPlots`ErrorBar@@{#3,#4}}&@@@OrganizedFiveMolar;
OrganizedTenMolar = {{#1,#2},ErrorBarPlots`ErrorBar@@{#3}}&@@@OrganizedTenMolar;

(* Making your own plot markers. Info found at
http://mathematica.stackexchange.com/questions/56155/change-the-inner-color-of-markers *)
ngon[p_,q_]:=Polygon[Table[{Cos[2 Pi k q/p],Sin[2 Pi k q/p]},{k,p}]]
g1=Graphics[{EdgeForm[Black],Blue,Disk[{0,0},1]}]; (* circular marker *)
g2=Graphics[{EdgeForm[Black],Red,ngon[4,1]}];(* diamond marker *)
g3=Graphics[{EdgeForm[Black],Green,Polygon[{{1,0},{0,Sqrt[3]},{-1,0}}]}];(* triangle marker *)

Labels={"Watts Nickel","5mM","10mM"};
pointLegend= Placed[PointLegend[Labels,LegendMarkerSize->14],{xpos-0.074,ypos-0.19}];

ExperimentalResults =
ErrorListPlot[{OrganizedWatts,OrganizedFiveMolar,OrganizedTenMolar},PlotMarkers-
>Table[{s,0.04},{s,{g1,g2,g3}}],PlotStyle->{Blue,Red,Green}, Frame->True,FrameLabel-
>{xAxis,yAxis},PlotRange->{{0,60},{0,100}},PlotLegends->pointLegend,LabelStyle->labelStyle]
```

## Combine Plots

```
CombinedPlot =Show[{TheoreticalResults,ExperimentalResults},PlotRange -
>{{0,65},{0,110}},ImageSize->360,AspectRatio-> 1]

CombinedSubPlot =Show[{TheoreticalResults, ExperimentalResults},PlotRange-
>{{0,8},{0,30}},ImageSize->360,AspectRatio-> 1]
```

## Stress Equations

```
sigma=1004000((h(1-C1-C2(1/2+λo-Δo)))/√2hU Cos[w]+(h^2 ((1/2+λ-Δ)-C3(1/2+λo-Δo)))/
√2h³V Sin[w+y])^-1;
t350=Table[sigma,{λ,rall},{h,hh2}];
sig=Table[t350[[i,i]],{i,1,Length[t350]}] ;
Length[sig]
```

## Theoretical Stress Calculations & Plot

Ge350E241GPa ->241 GPa Ni modulus, 350um Ge wafer thickness

Ge350E201GPa ->201 GPa Ni modulus, 350um Ge wafer thickness

```
(* Copied from 'sig' variable when the E1 = 241 *)

Ge350E241GPa={2.942030548228612`*^10,6.363901173934319`*^9,…………,5.8150532075
43921`*^8,5.815578375326855`*^8};

(* Copied from 'sig' variable when the E1 = 201 *)

Ge350E201GPa={2.6374668420901985`*^10,5.716070194035542`*^9,………….,4.970020956
2966734`*^8,4.969814681374273`*^8};

Stress241GPa =Transpose[{hh2 10^6,Ge350E241GPa 10^-6}];

Stress201GPa =Transpose[{hh2 10^6,Ge350E201GPa 10^-6}];


yAxis = Style["Stress (MPa)",16,FontFamily->"Arial"];

xAxis = Style["Nickel thickness (μm)",16,FontFamily->"Arial"];

xpos = 0.68; (* x-position of legend *)

ypos = 0.9; (* y-position of legend *)

swatchLegend = Placed[SwatchLegend[{"E_Ni = 221±20 GPa"},LegendMarkerSize-
>14],{xpos,ypos}];

labelStyle =Directive[FontFamily->"Arial",Black,FontSize->16];


TheoreticalResults = ListPlot[{Stress241GPa,Stress201GPa},Joined->True,PlotLegends->
swatchLegend,Filling->{1->{2},Top},FillingStyle->Opacity[0.7],PlotStyle-
>{Purple,Purple},Frame->True, FrameLabel->{xAxis,yAxis},PlotRange-
>{{0,60},{0,2500}},LabelStyle->labelStyle];


SpontSpallRegion = ListPlot[Stress241GPa,Joined->True,Filling->Top,FillingStyle-
>Opacity[0.2],PlotStyle->{Purple,Opacity[0.03]},Frame->True, FrameLabel-
>{xAxis,yAxis},PlotRange->{{0,60},{0,2500}},LabelStyle->labelStyle];


Show[{TheoreticalResults, SpontSpallRegion}]
```

## Experimental Stress Measurements (XRD)

```
FiveMolarRows = Range[7,19];

TenMolarRows = Range[46,52];

WattsRows = Range[78,92];


FolderPath = "C:\Users\.........\Plating Parameters.xlsx";
```

(* Create matrix data in the following order: Ni thickness, Ni Std Dev, Stress, Stress Std Dev *)

WattsData = Import[FolderPath,{"Sheets","Stress Analysis",WattsRows,{10,11,16,17}}];TenMolarData = Import[FolderPath,{"Sheets","Stress Analysis",TenMolarRows,{10,11,16,17}}];

FiveMolarData = Import[FolderPath,{"Sheets","Stress Analysis",FiveMolarRows,{18,19,24,25}}];

(* Sometimes we don't are left with rows of missing data. The rows are in the form of empty strings {"","","",""}. The command below removes those empty rows for plotting *)

FiveMolarData= DeleteCases[FiveMolarData,{"","","",""}];

Needs["ErrorBarPlots`"]

OrganizedWatts = {{#1,#3},ErrorBarPlots`ErrorBar@@{#2,#4}}&@@@ WattsData;OrganizedTenMolar = {{#1,#3},ErrorBarPlots`ErrorBar@@{#2,#4}}&@@@TenMolarData;OrganizedFiveMolar = {{#1,#3},ErrorBarPlots`ErrorBar@@{#2,#4}}&@@@FiveMolarData;

(* Making your own plot markers. Info found at http://mathematica.stackexchange.com/questions/56155/change-the-inner-color-of-markers *)

ngon[p_,q_]:=Polygon[Table[{Cos[2 Pi k q/p],Sin[2 Pi k q/p]},{k,p}]]

g1=Graphics[{EdgeForm[Black],Blue,Disk[{0,0},1]}]; (* circular marker *)

g2=Graphics[{EdgeForm[Black],Red,ngon[4,1]}];(* diamond marker *)

g3=Graphics[{EdgeForm[Black],Green,Polygon[{{1,0},{0,Sqrt[3]},{-1,0}}]}];(* triangle marker *)

pointLegend= Placed[PointLegend[Labels,LegendMarkerSize->14],{xpos-0.08,ypos-0.22}];

Labels={"Watts Nickel","5mM","10mM"};

ExperimentalResults = ErrorListPlot[{OrganizedWatts,OrganizedFiveMolar,OrganizedTenMolar},PlotMarkers->Table[{s,0.05},{s,{g1,g2,g3}}],PlotStyle->{Blue,Red,Green},

Frame->True,FrameLabel->{xAxis,yAxis},LabelStyle-> labelStyle,PlotRange->{{0,60},{0,2500}},PlotLegends->pointLegend ]

## Fitted Trend-line Approximation

CombinedData = Join[FiveMolarData, TenMolarData, WattsData];

f = NonlinearModelFit[CombinedData[[All,{1,3}]],a*x^n,{a,n},x];

f["RSquared"]

```
fittedLine = Plot[f[x],{x,0,100},PlotRange->{0,2500},PlotStyle->Red,Filling->Axis,FillingStyle->Opacity[0.07],PlotLegends->Placed[{"Fitted Line"},{0.75,0.35}]];
```

```
Show[ExperimentalResults,fittedLine]
```

## Combined Results

```
expre = Show[{TheoreticalResults,SpontSpallRegion,ExperimentalResults},ImageSize->330,AspectRatio->1]
```

## APPENDIX C MATLAB FILES FOR LASER PROFILOMETRY DEPTH ANALYSIS

```
%% PROFILOMETRYWRAPPER
% THIS SCRIPT CALCULATES THE AVERAGE SPALL DEPTH AND STD DEV FOR SAMPLES
% SCANNED BY NREL'S LASER PROFILOMETER. THE FILES MUST BE OF .XYZ TYPE AND
% FOLLOW A SPECIFIC NAMING CONVENTION TO BE IMPORTED CORRECTLY. THE FILES
% MUST BE IN THE SAME FOLDER, BEST TO NAME THE FOLDER THE SAME AS THE
% SAMPLE ID. LABEL REFERENCE PLANE FILES WITH 'Ref' AND SPALLED SURFACE
% FILES WITH 'Depth'. THE ONLY USER STEP IS TO SPECIFY WHICH FOLDER
% CONTAINS THE FILES TO BE ANALYZED. THE RESULTS ARE OUTPUT AS AN EXCEL
% FILE OF COMPILED RESULTS

%%
clc
clear
orig = pwd;

sampleID = 'Sphere Removal'; %Insert name of folder containing sample .xyz
files
cd(sampleID)

xyzFiles = dir('*.xyz'); %Find all .xyz files and save to structure field
[refMean, refStdDev, spalledMean, spalledStdDev] = deal(0); %preallocate
memory
for k = 1:length(xyzFiles)

    filename = xyzFiles(k).name; %Name of first file to be analyzed
    zData = dlmread(filename,',',0,2).*1000; %Read in z-values

    if 1 == ~isempty(strfind(filename,'Ref')) %Check if it's a reference
plane


        %Calc mean height and std dev
       % zData = zData(zData > -450);
        refMean = horzcat(refMean, mean(zData(:)));
        refStdDev = horzcat(refStdDev, std(zData(:)));

    elseif 1 == ~isempty(strfind(filename,'Depth')) %Check if it’s a spalled
surface

        %Calc mean height and std dev
        %zData = zData(zData > -450);
        spalledMean = horzcat(spalledMean, mean(zData(:)));
        spalledStdDev = horzcat(spalledStdDev, std(zData(:)));
    else
        disp('Some error occurred :[')
    end

end

meanSpallDepth = refMean(2)-spalledMean(2); %Average spall depth
```

```
variance = spalledStdDev(2).^2 + sum(refStdDev(2:end).^2);
meanStdDev = sqrt(variance); %Std dev of spall depth

disp(['The average spall depth for ', sampleID,' is ' num2str(meanSpallDepth)
' +/- ' num2str(meanStdDev) ' microns']);

headers = {'Sample ID' 'Ref Mean (um)' 'Ref Std Deviation (um)' 'Spalled Mean
(um)' 'Spalled Std Dev (um)' 'Mean Spall Depth (um)' 'Mean Std Dev (um)'};
outputVars = {sampleID refMean(2) refStdDev(2) spalledMean(2)
spalledStdDev(2) meanSpallDepth meanStdDev};
compiledResults = vertcat(headers,outputVars); %Compile the results in a
table with headers and results
fileName = horzcat(sampleID, ' Compiled Results');

xlswrite(fileName, compiledResults) %Export to excel within sample folder
cd(orig)
```